https://doi.org/10.5194/wes-2026-85
Preprint. Discussion started: 18 June 2026

eawe european academy of wind energy
Open Access WIND ENERGY SCIENCE DISCUSSIONS

Computationally efficient aerodynamic modeling of curved wind turbine blades and non-planar rotors using coupled near wake and vortex cylinder models

Ang Li[1], Mac Gaunaa[1], and Georg Raimund Pirrung[1]

[1]Department of Wind and Energy Systems, Technical University of Denmark, Frederiksborgvej 399, DK-4000 Roskilde, Denmark

Correspondence: Ang Li (angl@dtu.dk)

Abstract. Accurate aerodynamic modeling is essential for load calculation and optimization of modern wind turbine blades, which are increasingly flexible and may exhibit substantial sweep, prebend, coning, and deformation. Existing engineering models remain largely specialized to either sweep effects or prebend and non-planar effects, and therefore lack the ability to represent their combined influence within a single engineering formulation. This study develops a unified and computationally efficient framework for general curved and deformed blades by combining the coupled near and far wake model for swept blades with the vortex cylinder model for non-planar rotors. An idealized coupled formulation is first introduced as the highest-fidelity realization of the proposed framework before practical simplifications are introduced. Motivated by computational fluid dynamics (CFD) results showing that sweep and prebend effects can be modeled separately and then superimposed with good accuracy, simplified coupled models are then developed for practical applications. Comparisons with higher-fidelity free-wake lifting line (LL) and blade-resolved Reynolds-averaged Navier–Stokes (RANS) simulations show that the proposed models capture the aerodynamic load redistribution effects of curved blades with good accuracy across different blade configurations. In particular, for blades combining sweep and prebend, they close the gap between the previously separate sweep-only and prebend-only engineering approaches and provide clear improvements over existing specialized engineering models. The computational cost is higher than BEM but remains orders of magnitude lower than that of LL and CFD, making the simplified models attractive for time-domain aero-servo-elastic simulations and design optimization.

1 Introduction

The continuous advancement of wind turbine technology has led to significant increases in the size and flexibility of modern horizontal-axis wind turbine (HAWT) blades. By 2026, installed offshore wind turbines had reached rotor diameters of 300 m and rated power of 20 MW, while onshore turbines had reached rotor diameters of 266 m and rated power of 16.2 MW. This represents a dramatic leap from the 11 m rotor diameter of the Bonus 30 kW turbine introduced in the early 1980s. This evolution has driven interest in innovative blade designs, such as backward-swept blades for passive load alleviation through geometric bend-twist coupling (Liebst, 1986; Zuteck, 2002; Larwood and Zutek, 2006; Manolas et al., 2018), downwind rotor configurations with substantial downwind coning and prebend for low specific wind speed conditions (Madsen et al., 2020b),

https://doi.org/10.5194/wes-2026-85
Preprint. Discussion started: 18 June 2026

eawe european academy of wind energy
Open Access WIND ENERGY SCIENCE DISCUSSIONS

and aeroelastically optimized curved blade tip designs (Barlas et al., 2021). At the same time, similar aerodynamic challenges arise for rotors experiencing large flapwise deflections during operation, which is particularly relevant for ultra-long, highly flexible onshore wind turbine blades. Although unconventional and highly flexible blade configurations can offer aerodynamic and aeroelastic benefits, they also introduce significant challenges for aerodynamic load calculation and design optimization. Accurately modeling the aerodynamic effects of complex blade and wake geometries, particularly for blades that combine sweep and prebend or experience large deflections, is essential to avoid large uncertainties in load predictions and unforeseen aeroelastic instabilities.

Existing engineering aerodynamic models have limited capability for such complex blade geometries. The blade element momentum (BEM) method remains the primary low-fidelity tool in aero-servo-elastic simulations and design optimization because of its simplicity and computational efficiency. However, it implicitly assumes a planar rotor with straight blades (Li et al., 2022a, 2024, 2025b), which restricts its ability to capture the aerodynamic effects of blade curvature or rotor coning (Li et al., 2022a, c; Barlas et al., 2022; Horcas et al., 2023). Although BEM often shows reasonable agreement with higher-fidelity models for rotor-integral quantities such as thrust, power, or blade root bending moment, its inability to model either sweep or prebend effects, particularly the local load distributions, remains a significant limitation. Higher-fidelity methods, such as free-wake lifting line (LL) solvers and fully-resolved computational fluid dynamics (CFD) simulations using Reynolds-averaged Navier–Stokes (RANS) solvers, can model these effects with high accuracy. However, they are computationally intensive and impractical for iterative design and optimization processes. Consequently, they are typically used as references or for selected load cases.

To address these limitations, a number of extensions to the BEM framework have been proposed to account for the influence of blade and wake geometry on the inductions. However, these developments have largely followed two separate engineering branches. One branch focuses on prebend and non-planar effects. Crawford (2006) used the vortex cylinder model within the BEM framework to model prebend and coning effects. Branlard and Gaunaa (2015a) demonstrated the similarity between the BEM method and the superposition of vortex cylinders for planar rotors. Building on this, Li et al. (2022a) employed the blade element vortex cylinder (BEVC) model to relax the planar rotor assumption by making the starting positions of the vortex cylinders follow the axisymmetric surface swept by the blades. This formulation enables the modeling of prebend and coning effects and shows good agreement with higher-fidelity LL and RANS CFD simulations (Li et al., 2022a), but the influence of the finite number of blades is still modeled using Prandtl's empirical tip-loss correction. The other branch focuses on sweep effects. Fritz et al. (2022) introduced a simplified correction to Prandtl's tip-loss correction to account for blade sweep while retaining annular independence. Another approach is the coupled near and far wake model introduced by Madsen and Rasmussen (2004), in which the near wake is modeled using non-expanding helical vortex filaments and the far wake is modeled in simplified form. Further developments (Li et al., 2018, 2022c) extended the model to include sweep effects through modified trailed vortex geometry and also included the influence of the curved bound vortex (Li et al., 2020). The far wake is modeled using either momentum theory (Madsen and Rasmussen, 2004; Pirrung et al., 2016) or a far wake vortex cylinder formulation (Li et al., 2025a). This coupled near and far wake framework effectively captures blade sweep effects and shows good agreement with higher-fidelity LL and RANS CFD simulations for swept blades (Li et al., 2022c, 2025a).

https://doi.org/10.5194/wes-2026-85
Preprint. Discussion started: 18 June 2026

eawe european academy of wind energy
Open Access WIND ENERGY SCIENCE DISCUSSIONS

Despite these advances, neither branch alone provides a unified engineering model for general curved blades that combine sweep and prebend.

Building on these two parent branches, the present study proposes a unified aerodynamic modeling framework that integrates the coupled framework for swept blades (Li et al., 2025a) with the vortex cylinder model for non-planar rotors (Li et al., 2022a). The objective is not merely to further refine existing engineering models, but to close the capability gap for blades that combine sweep and prebend. To establish the theoretical upper limit of the proposed framework, an idealized coupled model is first introduced. In this formulation, the near wake explicitly models the combined effects of sweep and prebend, while the far wake accounts for non-planar effects using the vortex cylinder model. Although this formulation achieves high accuracy, it requires numerical integration at each iteration and is therefore computationally expensive. Motivated by recent CFD results showing that sweep and prebend effects can be modeled separately and then superimposed with good accuracy (Li et al., 2025b), simplified coupled models are also developed for practical applications. In these models, the existing near wake formulation is retained to capture sweep effects, while the vortex cylinder model accounts for prebend and coning effects. Two variants are considered. In the first, the far wake is modeled using the vortex cylinder model. In the second, the vortex cylinder model is used as a correction to the existing coupled near wake and far wake momentum theory to include non-planar effects. The latter formulation is particularly suitable for implementation in time-domain aeroelastic simulation tools, such as HAWC2 (Larsen and Hansen, 2007) and OpenFAST (Jonkman and Sprague, 2021). The procedure used to couple the near wake and far wake is also refined in the present work. The coupling factor determines how the total wake-induced velocity is partitioned between the near wake and far wake contributions. The rotor averaged coupling factor is determined from a corresponding planar reference rotor with straight blades, hereafter referred to as the auxiliary reference rotor. In this way, the coupling factor represents the wake partition itself, rather than compensating for induction effects caused by the sweep or prebend of the actual blade. Results from the proposed methods are compared against higher-fidelity LL and CFD simulations for various blade configurations, including swept blades, prebent blades, and blades with combined sweep and prebend. The proposed models demonstrate good agreement with higher-fidelity LL and CFD simulations while being orders of magnitude more computationally efficient. A detailed comparison of computational cost for planar rotors is provided in Li et al. (2025a), which is also representative of the present work.

This unified modeling framework represents a significant advancement in the efficient and accurate calculation of aerodynamic loads for non-straight blades and coned rotors. It establishes a practical engineering framework for general curved blades with combined sweep and prebend. The proposed framework can be used to replace the standard BEM induction calculation in aerodynamic and aero-servo-elastic simulation tools, while retaining compatibility with existing engineering submodels. It therefore has important implications for load prediction and design optimization of future wind turbine blades.

The remainder of this manuscript is structured as follows: Section 2 applies the Kutta–Joukowski theorem to analyze the aerodynamic effects of general curved blades. Section 3 summarizes the blade element vortex cylinder (BEVC) method for modeling prebend effects, while Section 4 reviews the coupled near and far wake model for swept blades. Section 5 introduces the idealized unified coupled model, and Section 6 presents the simplified coupled models for practical applications. Section 7 discusses the calculation of the coupling factor. Section 8 describes the simulation setup and blade geometries used for

https://doi.org/10.5194/wes-2026-85
Preprint. Discussion started: 18 June 2026

eawe european academy of wind energy
Open Access WIND ENERGY SCIENCE DISCUSSIONS

comparison. Section 9 presents results, including comparisons with higher-fidelity simulations. Finally, Section 10 concludes the manuscript with a summary of the findings, a discussion of their implications, and suggestions for future work.

2 Kutta–Joukowski analysis of a generalized curved blade

This section briefly summarizes the geometric notation required for the coupled models developed later and applies the Kutta–Joukowski (KJ) theorem to examine how the axial, tangential and radial induction components affect the aerodynamic loads of generalized curved blades with a prescribed circulation distribution. Full coordinate transformations and related derivations for generalized curved blades were presented in previous works (Li et al., 2024, 2025b). Here, only the quantities required for the present formulation are summarized.

Using the three-dimensional vector form of the KJ theorem (Okulov et al., 2015), the lift force is calculated from the bound circulation vector and the total velocity vector. The KJ analysis focuses on the lift force contribution to the aerodynamic loads, while profile drag and sectional moment are included afterwards as post-processing terms.

Previous studies have used KJ analysis to guide model development for planar, swept and prebent rotors (Branlard and Gaunaa, 2015a; Li et al., 2022a). For generalized curved blades, it has also been shown that the conventional BEM method cannot capture the influence of blade geometry on induction components (Li et al., 2024, 2025b). In this study, the KJ analysis is used to highlight the importance of accurately modeling each induction component for aerodynamic load calculations.

2.1 Coordinate systems

Three coordinate systems are used in the present work, as illustrated in Fig. 1: the sectional coordinate system (S-sys), the blade root coordinate system (B-sys) and the blade local coordinate system (BL-sys). The S-sys defines the local 2-D airfoil in the $x^{\mathrm{S}} - y^{\mathrm{S}}$ plane, with the z^{S}-axis tangent to the blade main axis. This system does not rotate with the blade twist angle. The B-sys has its origin on the rotational axis and rotates with the blade. Its y^{B}-axis is aligned with the free stream direction (axial direction), and its z^{B}-axis is aligned with the radial direction at the blade root. At each spanwise location, the BL-sys is obtained by rotating the B-sys about the y^{B}-axis such that the calculation point lies on the local radial z^{BL}-axis. Accordingly, the x^{BL}-axis represents the local tangential direction.

The blade geometry is described in B-sys. The local sweep angle ψ and dihedral angle κ are defined from the tangent vector $\boldsymbol{t}$ of the blade main axis:

$$\boldsymbol{t} = \begin{pmatrix} \frac{\mathrm{d}x^{\mathrm{B}}}{\mathrm{d}z^{\mathrm{B}}} \\ \frac{\mathrm{d}y^{\mathrm{B}}}{\mathrm{d}z^{\mathrm{B}}} \\ 1 \end{pmatrix} = \begin{pmatrix} -\tan\psi \\ -\tan\kappa \\ 1 \end{pmatrix}. \tag{1}$$

The transformation from B-sys to BL-sys is a rotation about the y-axis:

$$\mathbf{T}_{\mathrm{B}\to\mathrm{BL}} = \mathbf{R}_{\mathbf{y}}(\delta), \tag{2}$$

https://doi.org/10.5194/wes-2026-85
Preprint. Discussion started: 18 June 2026

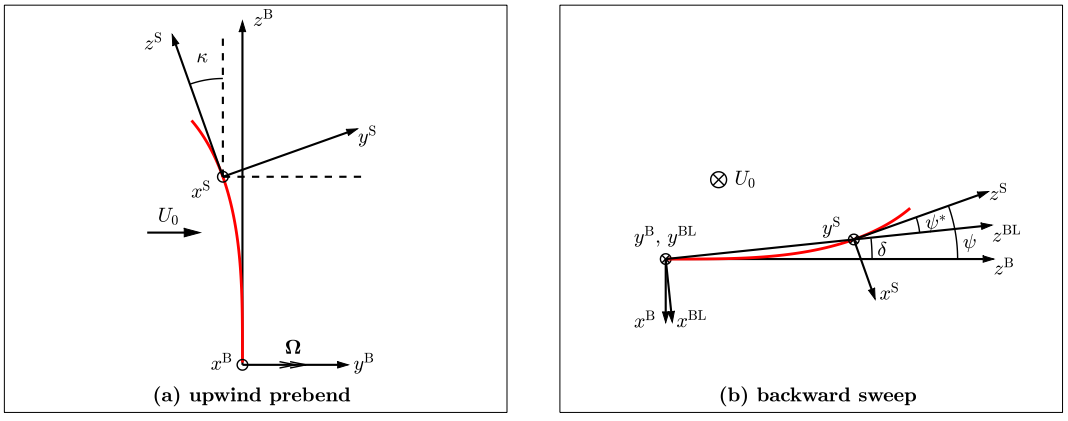

Figure 1. Illustration of the coordinate systems used in the present work. In (a), a blade with only upwind prebend is shown. In (b), a blade with only backward sweep is shown. The figure also illustrates the local sweep angle ψ, the dihedral angle κ, the position angle δ, and the effective sweep angle ψ^*. The figure is adapted from (Li et al., 2025b).

where the position angle δ is defined as

$$\tan\delta = -\frac{x^{\mathrm{B}}}{z^{\mathrm{B}}}. \tag{3}$$

It is convenient to introduce the effective sweep angle ψ^* and effective dihedral angle κ^* in BL-sys. The corresponding local tangent vector is

$$\boldsymbol{t}^* = \begin{pmatrix} -\tan\psi^* \\ -\tan\kappa^* \\ 1 \end{pmatrix} = \begin{pmatrix} -\tan(\psi-\delta) \\ -\dfrac{\tan\kappa\cos\psi}{\cos(\psi-\delta)} \\ 1 \end{pmatrix}. \tag{4}$$

These geometric quantities are sufficient for the KJ analysis and the coupled models introduced later. Full derivations of the coordinate transformations and related geometric relations are given in Li et al. (2024, 2025b).

2.2 Aerodynamic loads due to lift force

For a blade section of a clockwise rotating rotor as seen from upwind, the lift force is obtained from the three-dimensional Kutta–Joukowski (KJ) theorem. In the blade local coordinate system (BL-sys), the bound circulation vector is aligned with the local blade axis:

$$\boldsymbol{\Gamma}_{\mathrm{B}}^{\mathrm{BL}} = \frac{\boldsymbol{t}^*}{\|\boldsymbol{t}^*\|}\Gamma_{\mathrm{B}}. \tag{5}$$

The relative velocity vector $\boldsymbol{V}^{\mathrm{BL}}$ in BL-sys is determined by the axial, tangential and radial induced velocities, u_a, u_t and u_r, respectively. In BEM literature, the axial and tangential induced velocities are commonly expressed in terms of the induction

https://doi.org/10.5194/wes-2026-85
Preprint. Discussion started: 18 June 2026

eawe european academy of wind energy
Open Access WIND ENERGY SCIENCE DISCUSSIONS

factors a_B and a':

$$\boldsymbol{V}^{\mathrm{BL}} = \begin{pmatrix} -\Omega r + u_t \\ U_0 + u_a \\ u_r \end{pmatrix} = \begin{pmatrix} -\Omega r(1+a') \\ U_0(1-a_B) \\ u_r \end{pmatrix}, \tag{6}$$

where Ω is the rotational speed, r is the radial position and U_0 is the free-stream velocity.

The lift force on the blade section, expressed as force per unit span, then follows from:

$$\boldsymbol{f}_L^{\mathrm{BL}} = \rho \boldsymbol{V}^{\mathrm{BL}} \times \boldsymbol{\Gamma}_{\mathrm{B}}^{\mathrm{BL}}. \tag{7}$$

The local thrust and power coefficients from the KJ analysis are calculated from the total lift force of all N_{B} blades for an annulus of the actuator disc at radius r:

$$C_{t,\mathrm{KJ}} \equiv \frac{N_{\mathrm{B}} f_{L,y}^{\mathrm{BL}} \,\mathrm{d}s}{\frac{1}{2}\rho U_0^2 2\pi r \,\mathrm{d}r} = k_s \left(1 + a' - \frac{u_r}{U_0 \lambda_r} \tan\psi^*\right), \tag{8}$$

$$C_{p,\mathrm{KJ}} \equiv \frac{N_{\mathrm{B}} \Omega r f_{L,x}^{\mathrm{BL}} \,\mathrm{d}s}{\frac{1}{2}\rho U_0^3 2\pi r \,\mathrm{d}r} = k_s \left(1 - a_B + \frac{u_r}{U_0} \tan\kappa^*\right), \tag{9}$$

where k_s is the normalized circulation strength and λ_r is the local speed ratio at radius r, defined as:

$$k_s = \frac{\Omega N_{\mathrm{B}} \Gamma_{\mathrm{B}}}{\pi U_0^2}, \tag{10}$$

$$\lambda_r = \frac{\Omega r}{U_0}. \tag{11}$$

Note that the curved blade length correction with $\mathrm{d}s/\,\mathrm{d}r = \|\boldsymbol{t}^*\|$, where s denotes the blade span, is applied (Madsen et al., 2020a; Li et al., 2024, 2025b).

2.3 Influence of inductions on loads

For a curved blade with a prescribed circulation distribution, the influence of the inductions on the local thrust and power coefficients due to lift is analyzed from Eqs. (8) and (9). These equations are interpreted in two complementary ways. First, they show the *explicit* geometric contribution, namely whether the effective sweep angle ψ^* or effective dihedral angle κ^* appears directly in the load expressions. Second, they show the *wake-induced* contribution, namely how the induction terms a_B, a' and u_r modify $C_{t,\mathrm{KJ}}$ and $C_{p,\mathrm{KJ}}$. In this way, blade geometry can also influence the loads indirectly through its effect on the wake and hence on the inductions.

2.3.1 Explicit geometric contribution

Eqs. (8) and (9) can be decomposed into a baseline term and two terms with explicit geometric dependence, as summarized in Table 1.

https://doi.org/10.5194/wes-2026-85
Preprint. Discussion started: 18 June 2026

eawe european academy of wind energy
Open Access WIND ENERGY SCIENCE DISCUSSIONS

Table 1. Decomposition of the Kutta–Joukowski thrust and power coefficients into a baseline term and two terms with explicit geometric dependence.

Term	Contribution to $C_{t,\mathrm{KJ}}$	Contribution to $C_{p,\mathrm{KJ}}$	Explicit geometric dependence
Baseline term	$k_s(1+a')$	$k_s(1-a_B)$	None
Sweep-dependent term	$-k_s\dfrac{u_r}{U_0\lambda_r}\tan\psi^*$	–	ψ^* appears explicitly
Prebend-dependent term	–	$k_s\dfrac{u_r}{U_0}\tan\kappa^*$	κ^* appears explicitly

– Baseline term: This part contains no explicit ψ^* or κ^* dependence, so its mathematical form is the same for any blade geometry (straight, swept, prebent, or combined). In this sense, it serves as a common baseline in the KJ expressions. It also corresponds to the standard expressions for the local thrust and power coefficients when the radial induced velocity is neglected, as reported in previous studies (Li et al., 2025b, a). It should be noted, however, that the inductions a_B and a' still vary indirectly with blade geometry through wake-induced effects.

– Sweep-dependent term: The radial induced velocity u_r contributes to the thrust coefficient through the factor $\tan\psi^*$. Thus, sweep explicitly affects the local thrust through the combination of u_r and the effective sweep angle ψ^*. According to Eq. (8), when the local speed ratio λ_r is large, such as near the blade tip and at high tip-speed-ratio (TSR) conditions, the contribution of u_r to the thrust coefficient is relatively small. This behavior has also been observed for blades with sweep only using coupled near and far wake models (Li et al., 2025a).

– Prebend-dependent term: The radial induced velocity u_r contributes to the power coefficient through the factor $\tan\kappa^*$. Thus, prebend explicitly affects the local power through the combination of u_r and the effective dihedral angle κ^*. According to Eq. (9), this contribution is not divided by λ_r and can therefore remain significant under different operating conditions. Accurate modeling of u_r is thus particularly important for predicting the power of prebent blades.

2.3.2 Wake-induced effects on loads

Blade geometry also affects the aerodynamic loads indirectly through changes in wake geometry, which in turn influence the inductions. For rotors with curved blades or coned rotors, the inductions differ from those of straight blades forming a planar rotor (Li et al., 2020, 2022a, c).

– Axial induction a_B: As shown in Eq. (9), the axial induction factor a_B directly influences the power coefficient $C_{p,\mathrm{KJ}}$ through the baseline term. This highlights the importance of accurately modeling the effect of wake geometry on the axial induction.

– Tangential induction a': According to Eq. (8), the tangential induction factor a' directly influences the thrust coefficient $C_{t,\mathrm{KJ}}$, also through the baseline term. Since the magnitude of a' is typically much smaller than one, its influence is usually limited under normal operating conditions. Nevertheless, at lower TSR conditions it becomes more significant and should be modeled with higher accuracy.

https://doi.org/10.5194/wes-2026-85
Preprint. Discussion started: 18 June 2026

eawe european academy of wind energy
Open Access WIND ENERGY SCIENCE DISCUSSIONS

– Radial induced velocity u_r: According to Eqs. (8) and (9), the radial induced velocity u_r influences the thrust for swept blades and the power for prebent blades, respectively. Its effect is particularly important for prebent blades because it contributes directly to the power coefficient. For swept blades at high λ_r, however, its influence on thrust is relatively small, which allows further simplifications in modeling.

In summary, the KJ analysis shows that accurate modeling of the axial induction a_B is important for predicting power, particularly for curved blades. The tangential induction a' generally has a smaller influence, but becomes more relevant at lower TSR conditions. The radial induced velocity u_r is especially important for predicting power for prebent blades and should therefore be modeled with high accuracy, whereas its influence on thrust for swept blades is comparatively minor at high λ_r and allows greater simplification. These distinctions help explain why earlier engineering developments for sweep and for prebend/non-planar effects followed different modeling branches, and why a unified framework must combine their respective strengths.

3 Blade element vortex cylinder method

The blade element vortex cylinder (BEVC) method provides the non-planar/prebend parent branch used later in the unified framework. It combines blade element theory (BET) with the full trailed wake vortex cylinder (VC) model to account for non-planar effects on the axial and radial inductions (Crawford, 2006; Li et al., 2022a). For non-planar rotors, the force calculation requires additional care: in all models using 2-D airfoil data, the effective airfoil pitch rate should be accounted for when determining the magnitude and direction of the sectional forces (Li et al., 2022b). Only the ingredients required for the present unified formulation are summarized here. In the BEVC model, the full trailed wake is represented using concentric cylindrical vortex sheets, as described in Li et al. (2022a). The method can be viewed as a correction to the widely used blade element momentum (BEM) method. For planar rotors, if the pressure drop due to wake rotation is neglected, the BEVC method gives the same axial and tangential inductions as the BEM method (Branlard and Gaunaa, 2015b; Li et al., 2022a). In addition, the vortex cylinder representation provides a radial induction component, which is not part of the standard BEM formulation[1]. For non-planar rotors, however, the trailed vortices emanating from the blades have a different geometry from that of a planar rotor, since their starting positions are displaced in the streamwise direction following the curved axisymmetric surface swept by the blades. In the present work, the full trailed wake VC model is used in two ways. First, the BEVC method is included as a reference model in the numerical comparisons. Second, the full VC model provides the non-planar correction terms used later in the coupled models. However, by itself the BEVC method does not capture sweep-induced induction effects.

3.1 Elementary right vortex cylinder

The vortex cylinder model provides a simplified representation of the trailed vortex system generated by a rotor. For a planar rotor with a constant circulation distribution, operating under uniform inflow with zero yaw error and no rotor tilt, the vortex cylinder forms a right cylinder rather than an oblique one (Branlard and Gaunaa, 2015b).

[1]For planar rotors with straight blades, this radial induction does not contribute to the blade load calculation.

https://doi.org/10.5194/wes-2026-85
Preprint. Discussion started: 18 June 2026

eawe european academy of wind energy
Open Access WIND ENERGY SCIENCE DISCUSSIONS

The cylindrical vortex sheet has two components: the tangential vorticity γ_t, which contributes to both axial and radial induced velocities, and the longitudinal vorticity γ_l, which contributes to the tangential induced velocity only. For a vortex cylinder with radius R, the axial, radial and tangential induced velocities at a point with radius r and axial distance y (positive downstream from the rotor disc) are written as

$$u_a(r,y) = \tilde{u}_a(r,R,y)\gamma_t, \tag{12}$$

$$u_r(r,y) = \tilde{u}_r(r,R,y)\gamma_t, \tag{13}$$

$$u_{t,l}(r,y) = \tilde{u}_{t,l}(r,R,y)\gamma_l, \tag{14}$$

where $\tilde{u}_a$, $\tilde{u}_r$, and $\tilde{u}_{t,l}$ are functions involving complete elliptic integrals and their explicit forms are given in Branlard and Gaunaa (2015b); Li et al. (2025a).

3.2 Superposition of vortex cylinders

To represent a radially varying circulation distribution, the contributions from multiple concentric vortex cylinders are superpositioned (Branlard and Gaunaa, 2015a). For closure of the VC system, each cylindrical vortex sheet is assumed to convect at a constant speed given by the average of the velocities on the two sides of the sheet in the far wake (Branlard and Gaunaa, 2015a). For non-planar rotors, the system closure is performed using the corresponding planar rotor with the same circulation distribution (Li et al., 2022a).

For this corresponding planar rotor with straight blades, the Kutta–Joukowski thrust coefficient follows from Eq. (8) as

$$C_{t,\mathrm{KJ}}^{\mathrm{pl}} = k_s(1+a'). \tag{15}$$

The annulus-averaged axial induction factor [2] of the corresponding planar rotor, labeled a_∞^{pl}, is calculated from its effective thrust coefficient.

$$a_\infty^{\mathrm{pl}} = f_{a-C_t}(C_{t,\mathrm{eff}}^{\mathrm{pl}}) \tag{16}$$

This closure is not based on balancing the actual thrust force, as in a momentum theory framework. Instead, it uses the thrust coefficient of the corresponding planar rotor, which is equivalent to neglecting the contribution of radial induction to the thrust. In addition, the contribution of the drag to the thrust coefficient are neglected.

The effective thrust coefficient is the thrust coefficient from the KJ analysis minus the contribution of wake rotation pressure drop (Branlard and Gaunaa, 2015a; Li et al., 2022a). For typical modern wind turbine designs, this effect is rather small and may be neglected (Li et al., 2022a).

The tangential vorticity of each vortex cylinder is obtained from the jump in the planar annulus-averaged axial induction between two neighbouring sections (Li et al., 2022a):

$$\gamma_{t,j} = 2U_0(a_{\infty,j+1}^{\mathrm{pl}} - a_{\infty,j}^{\mathrm{pl}}). \tag{17}$$

[2] The annulus-averaged value corresponds to the limit of an infinite number of blades.

https://doi.org/10.5194/wes-2026-85
Preprint. Discussion started: 18 June 2026

eawe european academy of wind energy
Open Access WIND ENERGY SCIENCE DISCUSSIONS

When calculating the rotor-plane axial induction distribution used in Eq. 17, two auxiliary values outside the rotor radial range are introduced and set to $a^{\mathrm{pl}}_{\infty,0} = 0$ and $a^{\mathrm{pl}}_{\infty,N_{\mathrm{cp}}+1} = 0$.

The strength of the longitudinal vorticity of the vortex cylinder with radius R_j and total trailed wake strength $\Delta\Gamma_j$ is:

$$\gamma_{l,j} = -\frac{\Delta\Gamma_j}{2\pi R_j}. \tag{18}$$

At a calculation point with radius r and axial coordinate y, the contributions from all vortex cylinders are linearly superimposed to obtain the total axial and radial inductions:

$$a^{\mathrm{np}}_{\infty} = -\frac{1}{U_0}\sum_{j=1}^{N_{\mathrm{tp}}} \tilde{u}_a\left(r, R_j, y - y(R_j)\right)\gamma_{t,j}, \tag{19}$$

$$u^{\mathrm{np}}_{r} = \sum_{j=1}^{N_{\mathrm{tp}}} \tilde{u}_r\left(r, R_j, y - y(R_j)\right)\gamma_{t,j}. \tag{20}$$

The non-planar correction to the axial induction predicted by the full VC model is then defined as

$$\Delta a_{\mathrm{VC}} = a^{\mathrm{np}}_{\infty} - a^{\mathrm{pl}}_{\infty}. \tag{21}$$

The total tangential induction in the BEVC method, including the contributions from the bound vortex disc and the longitudinal vorticity of the trailed wake vortex cylinders, is obtained from the definition of circulation and is therefore equal to that of the corresponding planar rotor (Branlard and Gaunaa, 2015a; Li et al., 2022a).

$$a' = \frac{\Gamma}{4\pi\Omega r^2} = \frac{k_s}{4\lambda_r^2} \tag{22}$$

3.3 Blade element theory and tip-loss correction

For each vortex cylinder, the trailed vorticity strength is related to the bound circulation from the 2-D airfoil (blade element) of the two neighbouring blade sections, which is calculated from the lift coefficient C_L. Assuming all blades operate under the same conditions, the total bound circulation strength is

$$\Gamma = N_{\mathrm{B}}\Gamma_{\mathrm{B}} = \frac{1}{2}N_{\mathrm{B}}V_{\mathrm{rel}}cC_L. \tag{23}$$

The total strength of the vortices trailed into the wake is

$$\Delta\Gamma_j = \Gamma_j - \Gamma_{j-1}. \tag{24}$$

As in the BEM method, Prandtl's tip-loss correction F is applied to the axial induction to account for the effect of a finite number of blades (Glauert, 1935; Sørensen, 2016):

$$a^{\mathrm{pl}}_{B} = a_{\mathrm{BEM}} = f_{a-C_t}\left(C^{\mathrm{pl}}_{t,\mathrm{KJ}}/F\right), \tag{25}$$

$$F = \frac{2}{\pi}\cos^{-1}\left(\exp\left(-\frac{N_{\mathrm{B}}}{2}\frac{R_{\mathrm{tot}} - r}{r\sin\varphi}\right)\right). \tag{26}$$

https://doi.org/10.5194/wes-2026-85
Preprint. Discussion started: 18 June 2026

The inflow angle φ is calculated from the velocity locally at the blade section.

$$\tan\varphi = \frac{U_0(1-a_B)}{\Omega r(1+a')} \tag{27}$$

The axial induction of the non-planar rotor in the BEVC method is then obtained by applying the correction term in Eq. (21) to the planar BEM solution.

$$a_B^{\mathrm{np}} = a_B^{\mathrm{pl}} + \Delta a_{\mathrm{VC}} = a_{\mathrm{BEM}} + \Delta a_{\mathrm{VC}} \tag{28}$$

In summary, the axial, tangential and radial inductions of the BEVC method are calculated from Eqs. (28), (22) and (20), respectively. The rotor's non-planar effects are therefore included in both axial and radial inductions. However, the method does not account for blade sweep effects on the inductions, limiting its applicability for general curved blades that combine sweep and prebend.

4 Coupled near and far wake model for swept blades

This section summarizes the sweep-model ingredients required by the unified curved-blade formulation. The coupled near and far wake framework for swept blades was developed and compared with higher-fidelity LL and CFD results in previous work (Pirrung et al., 2016; Li et al., 2022c, 2025a); detailed derivations, sweep-only comparisons, and coupling-factor studies are therefore not repeated here.

As shown by the Kutta–Joukowski analysis in Sect. 2.2, accurate modeling of the sweep-induced inductions, particularly the axial induction, is essential for predicting the aerodynamic loads of swept blades. However, actuator-disc-based models such as BEM and BEVC remain radially independent for planar rotors, even when the blades are swept, and are therefore not able to capture the spanwise interactions introduced by blade sweep[3]. Moreover, Prandtl's empirical tip-loss correction is based on assumptions of straight blades and does not represent the actual circulation distribution and trailed-vortex geometry of swept blades.

The coupled near and far wake model (Madsen and Rasmussen, 2004; Pirrung et al., 2016) addresses these limitations by combining an explicit near wake model with a simplified far wake model. The *near wake*, defined as the first quarter revolution of the blade's own trailed vortex, is modeled explicitly using non-expanding helical vortex filaments. The *far wake*, which includes the remaining trailed wake of the blade itself and those of the other blades, is modeled in simplified form (Madsen and Rasmussen, 2004). A rotor-averaged coupling factor k_{FW} is used to couple the near and far wake contributions (Andersen et al., 2010; Pirrung et al., 2016), such that the resulting rotor thrust is comparable to that of a reference BEM model. The total axial and tangential inductions are written as

$$a_{B,\mathrm{tot}} = a_{\mathrm{NW}} + a_{\mathrm{FW}}, \tag{29}$$

$$a'_{\mathrm{tot}} = a'_{\mathrm{NW}} + a'_{\mathrm{FW}}. \tag{30}$$

[3]Only limited spanwise coupling from inner to outer sections remains through wake rotation.

https://doi.org/10.5194/wes-2026-85
Preprint. Discussion started: 18 June 2026

eawe european academy of wind energy
Open Access WIND ENERGY SCIENCE DISCUSSIONS

4.1 Near wake modeling of swept blades

For swept blades, the near wake model includes two key effects: the influence of the curved bound vortex and that of the trailed vortex with its shifted starting position within the rotor plane (Li et al., 2022c, 2025a). Importantly, both effects are required, since neglecting either leads to significant errors in the predicted sweep effects (Li et al., 2018). It is further assumed that the dominant sweep effects are captured by the bound vortex and the near trailed wake of the blade itself, whereas the contribution from the trailed wake of the other blades is negligible. Figure 2 illustrates these geometric quantities for a backward-swept blade.

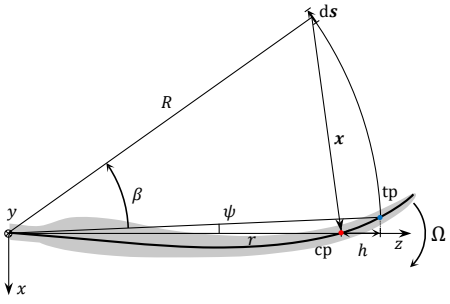

Figure 2. Front view of a backward swept wind turbine blade rotating clockwise, shown in the blade local coordinate system (BL-sys). The trailing point (tp) is at radius R and the calculation point (cp) is at radius r, with a radial difference h. The sweep angle ψ is the azimuthal difference between tp and cp. The difference in azimuthal angle between the elementary trailed vortex $\mathrm{d}\boldsymbol{s}$ and tp is β. The position vector $\boldsymbol{x}$ points from $\mathrm{d}\boldsymbol{s}$ to cp. This figure is adapted from Li et al. (2025a).

The near wake trailed vortex inductions are calculated using the computationally efficient indicial function approach described in Pirrung et al. (2016) and extended to swept blades in Li et al. (2022c, 2025a). Steady-state values are obtained from analytical expressions for special conditions and empirical corrections for general conditions, enabling high accuracy at low computational cost. In contrast, direct numerical integration of the Biot–Savart law would be significantly more expensive. The influence of the curved bound vortex is calculated separately using the Biot–Savart law, as detailed in Li et al. (2020).

The total near wake induction includes contributions from both the curved bound vortex and the near wake trailed vortex. The superscript (pl) indicates that the rotor is treated as planar, so sweep effects are included while non-planar effects are excluded.

$$a_{\mathrm{NW}}^{\mathrm{pl}} = a_{\mathrm{bound}} + a_{\mathrm{NW,\,trail}}^{\mathrm{pl}} \tag{31}$$

$$a_{\mathrm{NW}}^{\prime,\mathrm{pl}} = a_{\mathrm{bound}}^{\prime} + a_{\mathrm{NW,\,trail}}^{\prime,\mathrm{pl}} \tag{32}$$

4.2 Far wake model and coupling factors

The far wake is represented using either a momentum-theory-based model or a far wake vortex cylinder model (Li et al., 2025a). In both cases, the rotor-averaged coupling factor k_{FW} is used to couple the near and far wake contributions.

https://doi.org/10.5194/wes-2026-85
Preprint. Discussion started: 18 June 2026

eawe european academy of wind energy
Open Access WIND ENERGY SCIENCE DISCUSSIONS

4.2.1 Coupled with far wake momentum theory

In the momentum-theory-based far wake model, the rotor-averaged coupling factor k_{FW} directly scales down the full-wake inductions to obtain the far wake contribution. When combined with the near wake model, the resulting coupled model is labeled as NW-MT.

$$a_{\mathrm{FW,MT}} = f_{a-C_t}(k_{\mathrm{FW}} C_t) \tag{33}$$

$$a'_{\mathrm{FW,MT}} = k_{\mathrm{FW}} a' \tag{34}$$

The original automatically adjusted coupling factor method was developed for straight blades (Pirrung et al., 2016) and is insufficient for swept blades, particularly forward-swept blades (Li et al., 2022c). In the present work, NW-MT uses the area-weighted coupling-factor method (a) of Li et al. (2025a). Here, the method is modified by evaluating the coupling residual using an auxiliary reference rotor, defined as a corresponding planar rotor with straight blades, as described in Sect. 7.

The total axial and tangential inductions in the NW-MT model are obtained as

$$a_{B,\mathrm{tot}} = a_{\mathrm{NW}}^{\mathrm{pl}} + a_{\mathrm{FW,MT}}, \tag{35}$$

$$a'_{\mathrm{tot}} = a_{\mathrm{NW}}^{\prime,\mathrm{pl}} + a'_{\mathrm{FW,MT}}. \tag{36}$$

For the radial induction, NW-MT includes only the bound vortex contribution, since momentum theory does not provide a radial induction:

$$u_{r,\mathrm{tot}} = u_{r,\mathrm{bound}}. \tag{37}$$

4.2.2 Coupled with far wake vortex cylinder model

Alternatively, the far wake can be represented using vortex cylinders (Li et al., 2025a). When coupled with the near wake model, the resulting model is denoted NW-VC.

In this approach, the full trailed wake vortex cylinder is decomposed into a near wake part and a far wake part, as shown in Fig. 3(a). The far wake vortex cylinders are positioned at a constant distance Δy_{FW} downstream of the rotor plane. The sum of the inductions from the near wake and far wake vortex cylinders equals the inductions from the full vortex cylinder.

The downstream distance Δy_{FW} is taken as one-fourth of the area-weighted rotor-averaged near wake helical pitch $\hbar_{\mathrm{NW}}$ (Li et al., 2025a). This distance is further scaled by the rotor-averaged coupling factor k_{FW}, limited to values between 0 and 1, to reflect the reduced convection speed of the trailed wake compared to that at the rotor plane:

$$\Delta y_{\mathrm{FW}} = \frac{1}{4} k_{\mathrm{FW}} \hbar_{\mathrm{NW}}. \tag{38}$$

https://doi.org/10.5194/wes-2026-85
Preprint. Discussion started: 18 June 2026

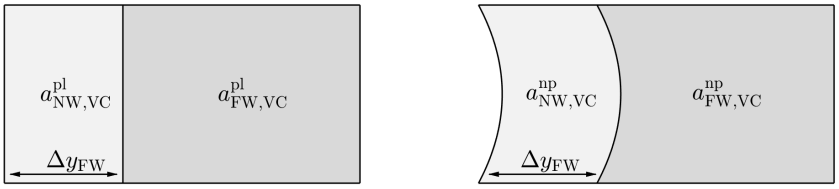

(a) Planar rotor (b) Non-planar rotor

Figure 3. Decomposition of the full trailed wake vortex cylinder into a near wake part and a far wake part for (a) a planar rotor and (b) a non-planar rotor.

For each calculation point, the far wake axial and tangential inductions are obtained by summing the contributions from all far wake vortex cylinders. When the rotor is planar, as indicated by the superscript (pl), the inductions at radius r are

$$a^{\mathrm{pl}}_{\mathrm{FW,VC}} = -\frac{1}{U_0}\sum_{j=1}^{N_{\mathrm{tp}}} \tilde{u}_a\left(r, R_j, -\Delta y_{\mathrm{FW}}\right)\gamma_{t,j}, \tag{39}$$

$$a'^{,\mathrm{pl}}_{\mathrm{FW,VC}} = -\frac{1}{\Omega r}\sum_{j=1}^{N_{\mathrm{tp}}} \tilde{u}_{t,l}\left(r, R_j, -\Delta y_{\mathrm{FW}}\right)\gamma_{l,j}. \tag{40}$$

For the radial induction, the treatment differs from that of the axial and tangential inductions. Because the existing helical near wake model does not provide the trailed wake contribution to radial induction, the trailed wake radial induction is taken directly from the full vortex cylinder model:

$$u^{\mathrm{pl}}_{r,\mathrm{VC}} = u^{\mathrm{pl}}_{r,\mathrm{NW,VC}} + u^{\mathrm{pl}}_{r,\mathrm{FW,VC}} = \sum_{j=1}^{N_{\mathrm{tp}}} \tilde{u}_r\left(r, R_j, 0\right)\gamma_{t,j}. \tag{41}$$

As in the BEVC model with full trailed wake vortex cylinders, each far wake vortex cylinder is assumed to convect at a constant axial velocity determined infinitely far downstream. Consequently, the far wake vortex cylinders are also solved using the corresponding planar full vortex cylinders. Once the vortex strengths γ_t and γ_l have been determined for the entire rotor, the far wake inductions can be evaluated.

For all coupled models using the far wake vortex cylinder model, we apply the area-weighted coupling-factor method (a), modified by evaluating the coupling residual using the auxiliary reference rotor described in Sect. 7.

The total inductions in the NW-VC model are then

$$a_{B,\mathrm{tot}} = a^{\mathrm{pl}}_{\mathrm{NW}} + a^{\mathrm{pl}}_{\mathrm{FW,VC}}, \tag{42}$$

$$a'_{\mathrm{tot}} = a'^{,\mathrm{pl}}_{\mathrm{NW}} + a'^{,\mathrm{pl}}_{\mathrm{FW,VC}}, \tag{43}$$

$$u_{r,\mathrm{tot}} = u_{r,\mathrm{bound}} + u^{\mathrm{pl}}_{r,\mathrm{VC}}. \tag{44}$$

Compared with NW-MT, NW-VC also includes the trailed wake contribution to the radial induction, whereas NW-MT includes only the bound vortex contribution.

https://doi.org/10.5194/wes-2026-85
Preprint. Discussion started: 18 June 2026

eawe european academy of wind energy
Open Access WIND ENERGY SCIENCE DISCUSSIONS

5 Idealized coupled model for blades with both sweep and prebend

Existing aerodynamic models capture either prebend effects through the vortex cylinder model (Sect. 3) or sweep effects through the coupled near and far wake framework (Sect. 4), but not their combined influence on general curved blades. To address this limitation, we introduce an idealized coupled model, denoted NW(ideal)-VC, as a benchmark formulation for blades with both sweep and prebend. It represents the highest fidelity achievable within the coupled modeling framework. For straight and swept blades, the same idealized-model concept reduces to the formulation used previously in Li et al. (2025a).

5.1 Near wake modeling

The near wake is defined as the first quarter revolution of the blade's own trailed wake and includes both sweep and prebend effects. The blade sweep geometry is described by the sweep angle ψ, while the blade prebend geometry is represented by the relative axial coordinate offset η between the trailing point (tp) at radius R and the calculation point (cp) at radius r:

$$\eta = y(R) - y(r). \tag{45}$$

Let β denote the trailed vortex azimuthal angle. The elementary trailed vortex vector $\mathrm{d}\boldsymbol{s}$ and the position vector $\boldsymbol{x}$ from $\mathrm{d}\boldsymbol{s}$ to the calculation point are:

$$\mathrm{d}\boldsymbol{s} = R\,\mathrm{d}\beta \begin{pmatrix} -\cos(\beta+\psi) \\ \tan\varphi \\ -\sin(\beta+\psi) \end{pmatrix}, \tag{46}$$

$$\boldsymbol{x} = \begin{pmatrix} R\sin(\beta+\psi) \\ -\eta - R\beta\tan\varphi \\ R - h - R\cos(\beta+\psi) \end{pmatrix}, \tag{47}$$

where $(h = R - r)$ is the radial difference between tp and cp, and φ is the inflow angle.

The elementary induced velocity follows from the Biot–Savart law:

$$\mathrm{d}\boldsymbol{w} = -\frac{\Delta\Gamma_{\mathrm{B}}}{4\pi}\frac{\boldsymbol{x}\times\mathrm{d}\boldsymbol{s}}{\|\boldsymbol{x}\|^3}. \tag{48}$$

Its axial, tangential and radial components, corresponding to the y-, x- and z-components of $\mathrm{d}\boldsymbol{w}$, are:

$$\mathrm{d}w_y^{\mathrm{np}} = -\frac{\Delta\Gamma_{\mathrm{B}}\,\mathrm{d}s\cos\varphi}{4\pi R^2}\frac{1-\tilde{r}\cos(\beta+\psi)}{\left[1+\tilde{r}^2-2\tilde{r}\cos(\beta+\psi)+(\beta\tan\varphi+\tilde{\eta})^2\right]^{\frac{3}{2}}}, \tag{49}$$

$$\mathrm{d}w_x^{\mathrm{np}} = \frac{\Delta\Gamma_{\mathrm{B}}\,\mathrm{d}s\cos\varphi}{4\pi R^2}\frac{\left[\tilde{r}-\cos(\beta+\psi)-\beta\sin(\beta+\psi)\right]\tan\varphi-\tilde{\eta}\sin(\beta+\psi)}{\left[1+\tilde{r}^2-2\tilde{r}\cos(\beta+\psi)+(\beta\tan\varphi+\tilde{\eta})^2\right]^{\frac{3}{2}}}, \tag{50}$$

$$\mathrm{d}w_z^{\mathrm{np}} = \frac{\Delta\Gamma_{\mathrm{B}}\,\mathrm{d}s\cos\varphi}{4\pi R^2}\frac{\left[\beta\cos(\beta+\psi)-\sin(\beta+\psi)\right]\tan\varphi+\tilde{\eta}\cos(\beta+\psi)}{\left[1+\tilde{r}^2-2\tilde{r}\cos(\beta+\psi)+(\beta\tan\varphi+\tilde{\eta})^2\right]^{\frac{3}{2}}}. \tag{51}$$

https://doi.org/10.5194/wes-2026-85
Preprint. Discussion started: 18 June 2026

eawe european academy of wind energy
Open Access WIND ENERGY SCIENCE DISCUSSIONS

where

$$\mathrm{d}s = V_{\mathrm{rel}}\,\mathrm{d}t = R\frac{\mathrm{d}\beta}{\cos\varphi}, \tag{52}$$

$$\tilde{r} = \frac{r}{R} = 1 - \frac{h}{R}, \tag{53}$$

$$\tilde{\eta} = \frac{\eta}{R}. \tag{54}$$

The steady-state near wake induced velocity is obtained by integrating the elementary contribution over the first quarter revolution, that is, from $\beta = 0$ to $\beta = \pi/2$:

$$\boldsymbol{W} = \int_{\beta=0}^{\beta=\frac{\pi}{2}} \mathrm{d}\boldsymbol{w}. \tag{55}$$

The total near wake induction includes contributions from both the bound vortex and the near wake trailed vortex. Here, the superscript (np) indicates that both sweep and prebend effects are included:

$$a_{\mathrm{NW}}^{\mathrm{np}} = a_{\mathrm{bound}} + a_{\mathrm{NW,trail}}^{\mathrm{np}}, \tag{56}$$

$$a_{\mathrm{NW}}^{\prime,\mathrm{np}} = a_{\mathrm{bound}}^{\prime} + a_{\mathrm{NW,trail}}^{\prime,\mathrm{np}}, \tag{57}$$

$$u_{r,\mathrm{NW}}^{\mathrm{np}} = u_{r,\mathrm{bound}} + u_{r,\mathrm{NW,trail}}^{\mathrm{np}}. \tag{58}$$

5.2 Far wake vortex cylinder model

The far wake is modeled using concentric vortex cylinders located downstream of the curved surface swept by the blades, as illustrated in Fig. 3 (b).

The same downstream shift distance Δy_{FW} as defined in Sect. 4.2.2 is used here. In this way, the far wake model includes non-planar effects while neglecting blade sweep effects. For a non-planar rotor, the far wake vortex cylinders do not start from one common axial position. Instead, each vortex cylinder is placed at a constant downstream distance Δy_{FW} relative to the local axial position of its corresponding blade trailing point.

The axial position (y-coordinate) of the far wake vortex cylinder at radius R_j is therefore obtained from the axial position of the corresponding trailing point (tp) on the blade at radius R_j and the downstream shift distance Δy_{FW}:

$$y_{\mathrm{FW},j} = y(R_j) + \Delta y_{\mathrm{FW}}. \tag{59}$$

https://doi.org/10.5194/wes-2026-85
Preprint. Discussion started: 18 June 2026

eawe european academy of wind energy
Open Access WIND ENERGY SCIENCE DISCUSSIONS

The far wake induced velocities at a calculation point with radius r and axial coordinate y are then computed by summing the contributions from all far wake vortex cylinders:

$$a_{\mathrm{FW,VC}}^{\mathrm{np}} = -\frac{1}{U_0}\sum_{j=1}^{N_{\mathrm{tp}}} \tilde{u}_a\left(r, R_j, y - y_{\mathrm{FW},j}\right)\gamma_{t,j}, \tag{60}$$

$$a_{\mathrm{FW,VC}}^{\prime,\mathrm{np}} = -\frac{1}{\Omega r}\sum_{j=1}^{N_{\mathrm{tp}}} \tilde{u}_{t,l}\left(r, R_j, y - y_{\mathrm{FW},j}\right)\gamma_{l,j}, \tag{61}$$

$$u_{r,\mathrm{FW,VC}}^{\mathrm{np}} = \sum_{j=1}^{N_{\mathrm{tp}}} \tilde{u}_r\left(r, R_j, y - y_{\mathrm{FW},j}\right)\gamma_{t,j}. \tag{62}$$

The total inductions are obtained by combining near- and far-wake contributions:

$$a_{B,\mathrm{tot}} = a_{\mathrm{NW}}^{\mathrm{np}} + a_{\mathrm{FW,VC}}^{\mathrm{np}}, \tag{63}$$

$$a_{\mathrm{tot}}^{\prime} = a_{\mathrm{NW}}^{\prime,\mathrm{np}} + a_{\mathrm{FW,VC}}^{\prime,\mathrm{np}}, \tag{64}$$

$$u_{r,\mathrm{tot}} = u_{r,\mathrm{NW}}^{\mathrm{np}} + u_{r,\mathrm{FW,VC}}^{\mathrm{np}}. \tag{65}$$

6 Simplified coupled model for blades with both sweep and prebend

While the idealized coupled model NW(ideal)-VC introduced in Sect. 5 provides a high-fidelity formulation for blades with both sweep and prebend, it is computationally too expensive for aeroelastic simulations and design optimization. The main cost arises from the near wake helical trailed-vortex model, which requires repeated direct numerical integration of the Biot–Savart law whenever blade deformation or operating conditions change.

For blades with sweep only, this cost is avoided by the computationally efficient near wake model described in Sect. 4.1, which combines analytical solutions for special flow conditions with approximations based on pre-calculated influence coefficients for general conditions. Extending that approach directly to include prebend would require a substantially more complex fitting procedure and a much larger database of steady-state near wake inductions, making it impractical.

Recent CFD results (Li et al., 2025b) showed that, for general curved blades, the wake-induced effects can be approximated well by modeling sweep and prebend separately and then linearly superimposing their contributions. Motivated by this result, we introduce two simplified coupled models: NW-VC and NW-MT-VC. Both retain the existing near wake trailed-vortex model for sweep effects and use the vortex cylinder model to account for prebend effects, thereby achieving a practical balance between computational efficiency and accuracy.

6.1 NW-VC: simplified near wake vortex cylinder model

The first simplified model, labeled NW-VC, is obtained by simplifying the idealized coupled model NW(ideal)-VC. For planar rotors, it reduces to the existing NW-VC model described in Sect. 4.2.2.

https://doi.org/10.5194/wes-2026-85
Preprint. Discussion started: 18 June 2026

eawe european academy of wind energy
Open Access WIND ENERGY SCIENCE DISCUSSIONS

6.1.1 Far wake model

The far wake is modeled using the same vortex cylinder formulation as in the idealized model NW(ideal)-VC, so the simplification introduced in NW-VC is limited to the near wake. The far wake vortex cylinders start at a constant downstream distance from the rotor plane, and the corresponding inductions are calculated from Eqs. (60) to (62).

6.1.2 Near wake model

In the near wake, sweep and prebend effects are modeled separately and then superimposed. Sweep effects are modeled by the existing computationally efficient near wake helical trailed vortex model described in Sect. 4.1. The non-planar contributions to the near wake axial and tangential inductions are modeled using the near wake part of the vortex cylinder. Specifically, they are calculated as the near wake vortex cylinder inductions of the non-planar rotor minus those of the corresponding planar rotor with the same circulation distribution. This treatment is analogous to the BEVC correction for non-planar effects in the full trailed wake described in Sect. 3.2.

The full vortex cylinder wake is decomposed into near wake and far wake parts, as illustrated in Fig. 3 (b). The near wake vortex cylinder inductions are then calculated by subtracting the far wake vortex cylinder inductions from the full vortex cylinder inductions:

$$a_{\mathrm{NW,VC}} = a_{\mathrm{VC}} - a_{\mathrm{FW,VC}}, \tag{66}$$

$$a'_{\mathrm{NW,VC}} = a'_{\mathrm{VC}} - a'_{\mathrm{FW,VC}}, \tag{67}$$

where a'_{VC} is the tangential induction from the longitudinal component of the full vortex cylinder, calculated using Eq. (14):

$$a'_{\mathrm{VC}} = -\frac{1}{\Omega r}\sum_{j=1}^{N_{\mathrm{tp}}} \tilde{u}_{t,l}\left(r, R_j, y - y(R_j)\right)\gamma_{l,j}. \tag{68}$$

Accordingly, the near wake axial and tangential inductions are written as the sum of the bound vortex term, the trailed wake induction term with sweep effects, and a vortex cylinder-based non-planar correction term. Since the simplified helical near wake model does not provide radial induction, the near wake radial induction is calculated from the bound vortex influence plus the near wake portion of the vortex cylinder:

$$a^{\mathrm{np}}_{\mathrm{NW}} = a_{\mathrm{bound}} + a^{\mathrm{pl}}_{\mathrm{NW,trail}} + a^{\mathrm{np}}_{\mathrm{NW,VC}} - a^{\mathrm{pl}}_{\mathrm{NW,VC}}, \tag{69}$$

$$a'^{,\mathrm{np}}_{\mathrm{NW}} = a'_{\mathrm{bound}} + a'^{,\mathrm{pl}}_{\mathrm{NW,\,trail}} + a'^{,\mathrm{np}}_{\mathrm{NW,VC}} - a'^{,\mathrm{pl}}_{\mathrm{NW,VC}}, \tag{70}$$

$$u^{\mathrm{np}}_{r,\mathrm{NW}} = u_{r,\mathrm{bound}} + u^{\mathrm{np}}_{r,\mathrm{NW,VC}}. \tag{71}$$

https://doi.org/10.5194/wes-2026-85
Preprint. Discussion started: 18 June 2026

eawe european academy of wind energy
Open Access WIND ENERGY SCIENCE DISCUSSIONS

6.1.3 Total inductions

The total inductions for NW-VC are obtained by summing the near wake and far wake contributions:

$$a_{B,\mathrm{tot}} = a^{\mathrm{np}}_{\mathrm{NW}} + a^{\mathrm{np}}_{\mathrm{FW,VC}} = a^{\mathrm{pl}}_{\mathrm{NW}} + a^{\mathrm{pl}}_{\mathrm{FW,VC}} + \Delta a_{\mathrm{VC}}, \tag{72}$$

$$a'_{\mathrm{tot}} = a'^{,\mathrm{np}}_{\mathrm{NW}} + a'^{,\mathrm{np}}_{\mathrm{FW,VC}} = a'^{,\mathrm{pl}}_{\mathrm{NW}} + a'^{,\mathrm{pl}}_{\mathrm{FW,VC}} + \Delta a'_{\mathrm{VC}}, \tag{73}$$

$$u_{r,\mathrm{tot}} = u_{r,\mathrm{bound}} + u^{\mathrm{np}}_{r,\mathrm{VC}}. \tag{74}$$

Here, the axial and tangential inductions consist of a planar part, denoted by the superscript pl, and a correction term accounting for non-planar effects. The non-planar correction terms Δa_{VC} and $\Delta a'_{\mathrm{VC}}$ are calculated as the full vortex cylinder inductions of the non-planar rotor minus those of the corresponding planar rotor. The axial correction is given by Eq. (21), while the tangential correction is calculated based on Eq. (68):

$$\Delta a'_{\mathrm{VC}} = a'^{,\mathrm{np}}_{\mathrm{VC}} - a'^{,\mathrm{pl}}_{\mathrm{VC}}. \tag{75}$$

Note that the non-planar contribution to the tangential induction predicted by the vortex cylinder model is relatively small. For all curved blades tested in this work, neglecting $\Delta a'_{\mathrm{VC}}$ changes the local thrust coefficient by less than 2×10^{-4} and the local power coefficient by less than 5×10^{-5}.

Compared to the idealized NW(ideal)-VC, the simplified NW-VC model approximates the sweep and prebend effects on the near wake inductions separately, instead of modeling them together using the helical trailed vortex. Based on previous CFD results (Li et al., 2025b), the resulting error is expected to be small for axial and tangential inductions. Larger discrepancies may occur for the radial induction because the influence of the finite number of blades is neglected.

6.2 NW-MT-VC: NW-MT corrected using vortex cylinder model

The second simplified coupled model, labeled NW-MT-VC, extends the existing NW-MT formulation to non-planar rotors. In NW-MT-VC, sweep effects are still modeled by the existing computationally efficient near wake helical trailed-vortex model. To account for non-planar effects, the inductions from the entire trailed wake, including both the near and far wake, are corrected using the vortex cylinder model. The trailed-wake radial induction is taken directly from the full vortex cylinder model, since it is not provided by the near wake helical trailed-vortex model. This NW-MT-VC model extends the earlier swept-blade approach of Li et al. (2025a) to non-planar rotors, while remaining consistent with that approach in the planar-rotor limit. The total inductions are therefore:

$$a_{B,\mathrm{tot}} = a^{\mathrm{pl}}_{\mathrm{NW}} + a_{\mathrm{FW,MT}} + \Delta a_{\mathrm{VC}}, \tag{76}$$

$$a'_{\mathrm{tot}} = a'^{,\mathrm{pl}}_{\mathrm{NW}} + a'_{\mathrm{FW,MT}} + \Delta a'_{\mathrm{VC}}, \tag{77}$$

$$u_{r,\mathrm{tot}} = u_{r,\mathrm{bound}} + u^{\mathrm{np}}_{r,\mathrm{VC}}. \tag{78}$$

Here, $a_{\mathrm{FW,MT}}$ and $a'_{\mathrm{FW,MT}}$ are the far-wake inductions from the momentum-theory model defined in Eqs. (33) and (34), while Δa_{VC} and $\Delta a'_{\mathrm{VC}}$ are calculated from the same expressions as in NW-VC in Sect. 6.1, namely Eqs. (21) and (75).

https://doi.org/10.5194/wes-2026-85
Preprint. Discussion started: 18 June 2026

eawe european academy of wind energy
Open Access WIND ENERGY SCIENCE DISCUSSIONS

For planar rotors, NW-MT-VC gives the same axial and tangential inductions as NW-MT, but additionally includes the radial induction. As in NW-VC, sweep and prebend effects are modeled separately and then superimposed. The main difference between the two simplified models lies in the modeling of the planar far wake contribution to the axial and tangential inductions: NW-MT-VC uses momentum theory, whereas NW-VC uses the far wake vortex cylinder model.

Similar to NW-VC, the error in NW-MT-VC compared to the idealized NW(ideal)-VC is expected to be small for axial and tangential inductions (Li et al., 2025b). Larger discrepancies may appear in the radial induction because the influence of the finite number of blades is not included.

7 Calculating the coupling factor

For all coupled models, a rotor-averaged coupling factor k_{FW} is used to partition the trailed wake into near- and far-wake contributions. In the present work, k_{FW} is determined from a corresponding planar reference rotor with straight blades, referred to as the auxiliary reference rotor, rather than from the actual rotor, which may include blade sweep, prebend, coning, or combinations of these features. This auxiliary reference rotor retains the same radial discretization, circulation distribution, and inflow angle as the actual rotor, but its blades are straight and have no non-planar offset. The superscript pl,str is used for quantities evaluated for this auxiliary reference rotor.

7.1 Planar reference rotor with straight blades

The near- and far-wake axial inductions of the auxiliary reference rotor are denoted $a_{\mathrm{NW}}^{\mathrm{pl,str}}$ and $a_{\mathrm{FW}}^{\mathrm{pl,str}}(k_{\mathrm{FW}})$, respectively. The far-wake induction is evaluated using the far-wake model of the corresponding coupled model. Thus, NW-MT and NW-MT-VC use the momentum-theory far-wake model, whereas NW-VC and NW(ideal)-VC use the vortex cylinder far-wake model.

The coupling factor is calculated using the area-weighted Newton procedure introduced as method (a) in Li et al. (2025a), but with the residual evaluated for the auxiliary reference rotor. For blade section i, the residual is

$$\delta a_i^{\mathrm{pl,str}} = a_{\mathrm{NW},i}^{\mathrm{pl,str}} + a_{\mathrm{FW},i}^{\mathrm{pl,str}}(k_{\mathrm{FW}}) - a_{\mathrm{BEM},i}. \tag{79}$$

Here, $a_{\mathrm{BEM},i}$ is the corresponding BEM reference axial induction, with tip-loss correction included. The residual function is then

$$F_a = \sum_{i=1}^{N_{\mathrm{cp}}} \delta a_i^{\mathrm{pl,str}} A_{a,i}, \tag{80}$$

where $A_{a,i}$ is the annular area corresponding to blade section i. The rotor-averaged coupling factor is updated from the previous step $t-1$ to the current step t as

$$k_{\mathrm{FW}}^{t} = k_{\mathrm{FW}}^{t-1} - \frac{F_a^t}{\partial F_a / \partial k_{\mathrm{FW}}}, \tag{81}$$

where

$$\frac{\partial F_a}{\partial k_{\mathrm{FW}}} = \sum_{i=1}^{N_{\mathrm{cp}}} \frac{\partial a_{\mathrm{FW},i}^{\mathrm{pl,str}}}{\partial k_{\mathrm{FW}}} A_{a,i}. \tag{82}$$

https://doi.org/10.5194/wes-2026-85
Preprint. Discussion started: 18 June 2026

eawe european academy of wind energy
Open Access WIND ENERGY SCIENCE DISCUSSIONS

As in method (a) of Li et al. (2025a), the Newton update is limited to avoid excessively large sectional errors. This limiting procedure is based on tentative sectional coupling factors; details are given in that work.

Because the residual is evaluated for the auxiliary reference rotor, sweep- and prebend-induced induction effects are not absorbed into k_{FW}. Instead, these effects are retained in the final induction calculation for the actual curved blade. This removes a major source of local residuals in the previous formulation, where induction effects associated with sweep were balanced against a BEM induction that does not include such effects.

8 Simulation setup and blades for comparison

This section summarizes the models, reference solvers, blade geometries, operating conditions, and load definitions used in the comparison.

8.1 Engineering aerodynamic models for comparison

Engineering aerodynamic models of different fidelities are included in the comparison. First, the BEM method described in Sect. 3 is used as the baseline, which does not model the influence of wake geometry on the loads. Second, the BEVC method, also described in Sect. 3, is included. It uses the vortex cylinder model for rotor non-planar effects but neglects the blade sweep effect on inductions. Third, the original coupled model NW-MT described in Sect. 4 is included for comparison. It models blade sweep effects but not rotor non-planar effects. Finally, the modified coupled models, including the idealized coupled model NW(ideal)-VC and the simplified coupled models NW-VC and NW-MT-VC, are used for comparison. These modified coupled models include both blade sweep and prebend effects. Unless otherwise stated, all coupled models in the present work use the improved method (a), based on the auxiliary reference rotor, to determine the rotor-averaged coupling factor. For clarity, the main characteristics and roles of these engineering aerodynamic models are summarized in Table 2.

Table 2. Summary of the engineering aerodynamic models considered in the present work. NW-MT-VC and NW-VC are the proposed models for application in aeroelastic simulation and optimization tools.

Model	Sweep	Prebend	Wake model	Radial induction	Role
BEM	No	No	MT / planar VC	No	Baseline
BEVC	No	Yes	VC	VC	Non-planar reference
NW-MT	Yes	No	NW + FW MT	Bound	Sweep reference
NW-MT-VC	Yes	Yes	NW + FW MT + ΔVC	Bound + VC	Simplified unified model
NW-VC	Yes	Yes	NW + FW VC + ΔVC	Bound + VC	Simplified unified model
NW(ideal)-VC	Yes	Yes	NW + FW VC	Bound + NW + FW VC	Idealized benchmark

For all cases, each blade is discretized radially into 80 sections. The airfoil data is from 2-D fully turbulent CFD results (Bortolotti et al., 2019); a setup analog to the CFD setup used for the reference 3-D blade-resolved CFD results. In this study,

https://doi.org/10.5194/wes-2026-85
Preprint. Discussion started: 18 June 2026

eawe european academy of wind energy
Open Access WIND ENERGY SCIENCE DISCUSSIONS

the relationship between the axial induction factor a and the thrust coefficient C_t, as used in Eqs. (33) and (16), follows the empirical polynomial formulation presented in (Madsen et al., 2020a).

8.2 High-fidelity reference: 3-D RANS solver

The pressure-based incompressible three-dimensional solver EllipSys3D was used as the high-fidelity reference. It solves the incompressible Reynolds-averaged Navier–Stokes (RANS) equations using a finite-volume discretization. The computational fluid dynamics (CFD) mesher and solver setups were identical to those used in Li et al. (2025a); therefore, only the key settings are summarized here. The outer CFD domain used an inlet/outlet boundary-condition strategy. The flow was assumed fully turbulent and modeled with the k-ω shear stress transport (SST) model (Menter, 1994). Rotor-resolved meshes were generated with the same structured blade-surface and radial extrusion workflow as in Li et al. (2025a). The outer boundary was located at approximately 11 rotor diameters. Boundary layer clustering targeted $y^+ < 1$, and the final volume mesh contained 14.2 million cells. As in Li et al. (2025a), a steady solver was employed and the reported blade loads were averaged over the last 50 iterations. Some error therefore remained in the blade root region, where unsteady separation is expected. Applying convergence enhancement methods to the RANS CFD solver, such as the modified BoostConv method (Dicholkar et al., 2022, 2025), could improve the root region comparisons. However, this does not affect the conclusions of the present study, which focus on the mid-span and blade tip regions.

8.3 Free-wake lifting line reference

In addition to the RANS CFD solver, the free-wake lifting line (LL) module implemented in the in-house multi-fidelity vortex code MIRAS (Ramos-García et al., 2016, 2017) is used as another higher-fidelity aerodynamic reference. In contrast to the blade-resolved RANS CFD approach that resolves the 3-D flow field around the blade geometry, the LL method relies on 2-D airfoil data and the cross-flow principle (Hoerner and Borst, 1985). It thus represents the highest fidelity within the framework of engineering aerodynamic models that rely on 2-D airfoil data, and therefore provides the most direct reference for the comparisons. The LL setup is identical to that used in Li et al. (2025a); therefore, only the key modeling details and numerical settings relevant to the present study are summarized here. Each blade is represented by a concentrated bound vortex line located at the 1/4 chord line, from which vorticity is trailed and shed into a free wake. The influence of a curved bound vortex on itself is included (Li et al., 2020). The vortex system of the blades and the wake is modeled using the same hybrid filament-particle-mesh approach as in Li et al. (2025a). The bound vortex and the first 360 wake panels behind each blade, corresponding to approximately 1.5 rotor revolutions, are represented by vortex filaments, while the remaining wake is represented by vortex particles on an auxiliary Cartesian mesh. The Cartesian mesh used for wake modeling spans approximately $(11D \times 2D \times 2D)$, where D is the rotor diameter, with a cell size of 2.5 m, corresponding to approximately $0.0125D$. This gives approximately 22.5 million cells and an equal number of vortex particles.

A time step of 0.03 s is used, corresponding to an azimuthal discretization of approximately 1.5°, or 240 time steps per rotor revolution. Each simulation is run for 20,000 time steps, corresponding to 600 s of physical time or approximately 83 rotor revolutions. A maximum of 50 sub-iterations is applied at each time step to ensure convergence of the angle of attack residual.

https://doi.org/10.5194/wes-2026-85
Preprint. Discussion started: 18 June 2026

eawe european academy of wind energy
Open Access WIND ENERGY SCIENCE DISCUSSIONS

Each blade is discretized radially into 50 spanwise sections using cosine spacing. The airfoil polars are obtained from fully turbulent 2-D RANS CFD simulations (Bortolotti et al., 2019).

8.4 Blades used for the comparison

All blades considered in the present work are based on the IEA-10.0-198 10 MW reference wind turbine (RWT) (Bortolotti et al., 2019). The baseline straight blade and the parameterization of the curved blades follow previous works (Li et al., 2018, 2022a, c, 2025a, b). The baseline straight blade is obtained by aligning the half-chord line with a straight main axis. The modified curved blades introduced in Li et al. (2025b) are used in the present study. For these blades, the chord and twist distributions are adjusted such that the BEM method predicts the same circulation distribution and almost identical loads as for the baseline straight blade, except for small residual differences due to drag projection. This largely removes the projection effect and allows the present comparisons to focus on the influence of wake geometry on the inductions and the resulting loads (Li et al., 2025b).

The curved main axis geometry is defined in the blade root coordinate system (B-sys) using a modified Bézier curve, parameterized by the curve ratio $\bar{r}_c$, the curve magnitude Δd, and the tip curve angle Λ_{tip}, as shown in Fig. 4. The detailed comparisons presented here focus on one representative parameter set, namely $\bar{r}_c = 0.5$, $\Delta d = 0.1$ and $\Lambda_{tip} = 20°$, as defined in Li et al. (2025b). Blade sweep and prebend are introduced by modifying the x^{B}- and y^{B}-coordinates of the main axis, respectively. For blades containing sweep, the main axis is further scaled so that the radius of each blade section remains identical to that of the baseline straight blade.

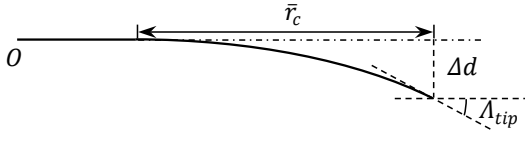

Figure 4. Parameterization of the curved blade with curve ratio $\bar{r}_c$, curve magnitude Δd and tip curve angle Λ_{tip}, adapted from Li et al. (2025b).

Following Li et al. (2025b), the modified swept blades are denoted mB-b, the modified prebent blades mW-w, and the modified combined blades mC-bw. For the representative parameter set used here, the two swept blades are mB-1 and mB-5, corresponding to backward and forward sweep, respectively, as illustrated in Fig. 5. The two prebent blades are mW-1 and mW-5, corresponding to upwind and downwind prebend, respectively, as illustrated in Fig. 6. These figures are adapted from Li et al. (2025b) and are included here to define the sign conventions used throughout the present study.

The combined curved blades are constructed by superimposing the corresponding swept and prebent planforms. For the representative parameter set, four combined cases are considered here, covering all combinations of sweep and prebend directions for this specific shape. Blade mC-11 has backward sweep and upwind prebend, blade mC-55 has forward sweep and downwind prebend, blade mC-15 has backward sweep and downwind prebend, and blade mC-51 has forward sweep and upwind prebend.

https://doi.org/10.5194/wes-2026-85
Preprint. Discussion started: 18 June 2026

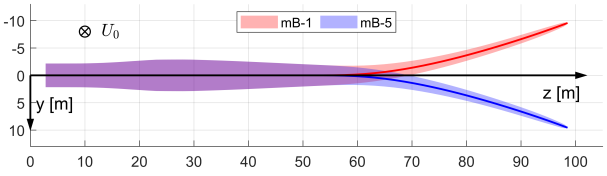

Figure 5. Front view of the backward swept blade mB-1 and the forward swept blade mB-5, with main axes highlighted, in the blade root coordinate system (B-sys). This corresponds to the front view of the rotor when the blade is pointing to the east. The free wind velocity vector is also shown. The figure is adapted from (Li et al., 2025b).

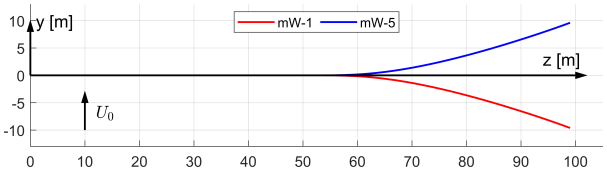

Figure 6. The main axis geometries of the upwind prebent blade mW-1 and the downwind prebent blade mW-5, in the blade root coordinate system (B-sys). This corresponds to the top view of the rotor when the blade is pointing to the east. The free wind velocity vector is also shown. The figure is adapted from (Li et al., 2025b).

The swept blades mB-1 and mB-5 are the same blade geometries as those used in Li et al. (2025a) and serve as limiting cases connecting the present generalized framework to the earlier swept-blade work. However, because the coupling-factor calculation is further improved here using the auxiliary reference rotor introduced in Sect. 7, the coupled model predictions for these swept blades are updated. Selected sweep-only results are therefore repeated to document the effect of the revised coupling-factor definition and to support the use of method (a) as the default coupling-factor procedure in the present generalized framework.

To examine the generality of the conclusions, a total of four distinct curved-blade shapes are considered, as defined in Li et al. (2022c, 2025b). For each shape, two sweep-only blades and two prebent-only blades are defined, giving 8 swept blades and 8 prebent blades in total. By combining these swept and prebent blades, a total of 64 combined curved blade cases is obtained. The detailed comparisons presented here focus on the 2 swept blades, 2 prebent blades and 4 combined curved blades derived from one representative shape. The internet appendix (Li et al., 2026) provides the complete set of results for the remaining geometries not shown in the main text. These extended results show trends consistent with those discussed here and do not change the overall conclusions of the present study.

For all test cases, the rotor radius is 99 m with a hub radius of 2.8 m. The blades are assumed to be stiff, so elastic deformation effects are not included.

https://doi.org/10.5194/wes-2026-85
Preprint. Discussion started: 18 June 2026

eawe european academy of wind energy
Open Access WIND ENERGY SCIENCE DISCUSSIONS

8.5 Operational conditions

The rotor's operational conditions are identical to those used in previous works (Li et al., 2022a, b, c, 2025a) and are restated here for completeness. An optimal operating condition with high rotor thrust is included, with a uniform inflow of 8 $\mathrm{m\,s^{-1}}$ perpendicular to the rotor plane, a rotational speed of 0.855 $\mathrm{rad\,s^{-1}}$ and zero blade pitch. The rotor radius is 99 m and the tip-speed-ratio (TSR) is 10.58. In addition, three lower-loading conditions defined in the IEA Wind TCP Task 37 report (Bortolotti et al., 2019) are considered, with rotational speed fixed at 0.909 $\mathrm{rad\,s^{-1}}$, wind speed varying from 12.0 $\mathrm{m\,s^{-1}}$ to 20.0 $\mathrm{m\,s^{-1}}$, and the straight blade is pitched towards lower loading. The curved blades are not directly pitched; instead, their chord and twist distributions are modified according to Li et al. (2025b), such that the BEM method predicts approximately the same loads as for the corresponding pitched straight blade. The main axis geometry of the curved blades remains unchanged from the optimal operating condition.

The operating conditions are summarized in Table 3, together with the thrust and power coefficients of the rotors with baseline straight blades predicted by the CFD solver.

Table 3. Operational conditions used for the comparison. $C_{T,\mathrm{CFD}}^{\mathrm{str}}$ and $C_{P,\mathrm{CFD}}^{\mathrm{str}}$ are the thrust and power coefficients of the rotor with baseline straight blades, as predicted by the CFD solver.

Wind speed U_0 [$\mathrm{m\,s^{-1}}$]	Tip-speed-ratio λ [-]	Pitch angle θ_p [°]	$C_{T,\mathrm{CFD}}^{\mathrm{str}}$ [-]	$C_{P,\mathrm{CFD}}^{\mathrm{str}}$ [-]
8.0	10.58	0.00	0.90	0.45
12.0	7.50	5.98	0.42	0.31
15.0	6.00	11.77	0.21	0.16
20.0	4.50	18.51	0.09	0.07

8.6 Loads for comparison

The loads used for comparison are identical to those used in Li et al. (2025a). The non-dimensional axial and tangential loads, which are in the y- and x-directions in the blade local coordinate system (BL-sys), are used for comparison. They are expressed in terms of the local thrust coefficient and the simplified local power coefficient:

$$C_t = \frac{N_\mathrm{B} f_y^{\mathrm{BL}} \,\mathrm{d}s}{\frac{1}{2}\rho U_0^2 2\pi r \,\mathrm{d}r}, \tag{83}$$

$$\tilde{C}_p \equiv \frac{\Omega r N_\mathrm{B} f_x^{\mathrm{BL}} \,\mathrm{d}s}{\frac{1}{2}\rho U_0^3 2\pi r \,\mathrm{d}r}. \tag{84}$$

Here, f^{BL} denotes force per unit span length and includes both lift and drag forces. The quantity $\tilde{C}_p$ represents the contribution of the tangential force to aerodynamic power; other contributions, such as sectional moments, are not included.

https://doi.org/10.5194/wes-2026-85
Preprint. Discussion started: 18 June 2026

eawe european academy of wind energy
Open Access WIND ENERGY SCIENCE DISCUSSIONS

To highlight the influence of curved blade geometry on the loads, load offsets relative to the baseline straight blade are also used for the comparison:

$$\Delta C_t(r) = C_t(r) - C_t^{\mathrm{str}}(r), \tag{85}$$

$$\Delta \tilde{C}_p(r) = \tilde{C}_p(r) - \tilde{C}_p^{\mathrm{str}}(r). \tag{86}$$

9 Results

In this section, loads calculated from different aerodynamic models are compared for swept blades, prebent blades, and blades with combined sweep and prebend. The proposed coupled models, including the idealized coupled model NW(ideal)-VC and the simplified coupled models NW-VC and NW-MT-VC, are evaluated against the existing engineering aerodynamic models BEM, BEVC, and NW-MT, using higher-fidelity LL and CFD results as references.

Before discussing the individual blade cases, it is useful to clarify how the model comparisons are interpreted. The main focus is on the distributed local thrust and power along the blade span. Previous studies have shown that both sweep and prebend introduce spanwise load redistribution patterns (Li et al., 2022a, c, 2025a, b). Similar redistribution effects are therefore expected for general curved blades that combine sweep and prebend.

The rotor-integrated thrust and power reported in the tables are important global measures of aerodynamic performance. The rotor-integrated power coefficient differs from directly integrating the simplified local power coefficient $\tilde{C}_p$ used in the spanwise plots.[4] Similarly, other integrated loads, such as blade-root bending moments, are important for load assessment, although they are not reported here. However, these integrated quantities are not the only relevant measures in aerodynamic and aeroelastic evaluations. Distributed loads are also important for blade design optimization and load assessment. For example, when evaluating the bending moment at a specific blade section, the relevant load is the integrated contribution from the blade tip to that section, not only the total load over the entire blade. Consequently, local load errors can be larger than suggested by rotor-integrated quantities, because positive and negative spanwise errors may cancel during integration along the span.

The higher-fidelity LL and CFD results are used as complementary references, but they should not be interpreted in the same way. The LL solver represents the highest-fidelity reference within the class of engineering aerodynamic models that use 2-D airfoil polar data. It is therefore the most direct reference for assessing the performance of the proposed engineering models. The blade-resolved RANS CFD simulations, in contrast, resolve the 3-D flow around the blade geometry and are used as an independent high-fidelity comparison. Consequently, LL and CFD are expected to show consistent dominant curved blade spanwise load redistribution patterns, although some quantitative differences are expected because the two approaches rely on different aerodynamic modeling assumptions. Agreement with CFD alone should therefore not be used as the sole criterion for assessing the performance of the engineering models. Instead, the comparison focuses on whether the engineering models reproduce the spanwise redistribution trends indicated by the higher-fidelity approaches, with LL providing the most direct benchmark.

[4]The difference is mainly due to the additional moment associated with applying the sectional lift and drag forces at the 1/4 chord line rather than at the blade main axis. The contribution from the profile sectional moment is negligible in the present cases.

https://doi.org/10.5194/wes-2026-85
Preprint. Discussion started: 18 June 2026

eawe european academy of wind energy
Open Access WIND ENERGY SCIENCE DISCUSSIONS

9.1 Baseline straight blade

For completeness, Fig. 7 shows the loads of the baseline straight blade predicted by the BEM method and the coupled models NW-MT and NW-VC, together with results from the LL and CFD solvers. The straight blade is included as the reference for the subsequent load offset comparisons and as a consistency check that the present implementation recovers the expected straight-blade limit. For this case, results from BEVC, NW(ideal)-VC and NW-MT-VC are omitted, since for a planar rotor with straight blades they are nearly identical to BEM, NW-VC and NW-MT, respectively, for the loads considered here.

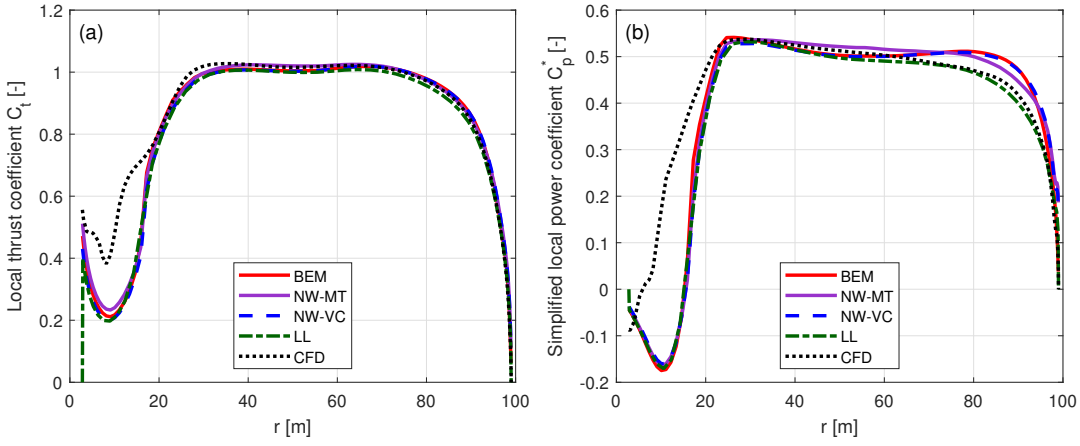

Figure 7. Thrust coefficient C_t (a) and simplified power coefficient $\tilde{C}_p$ (b) of the baseline straight blade at a wind speed of 8 m s^{-1}, calculated using the BEM method, the coupled methods NW-MT and NW-VC, the LL solver, and the CFD solver.

For radii less than 20 m, the CFD solver shows noticeable differences from the other methods for both axial and tangential loads. As discussed in Sect. 8, this discrepancy is related to unsteady flow separation in the blade root region. Therefore, the comparison focuses on the span from 20 m to the blade tip.

Over most of the span, the thrust coefficients predicted by the different models show good agreement. Larger differences appear in the simplified power coefficient near the outer blade region, where all engineering aerodynamic models over-predict the tangential load compared to the LL and CFD results. According to the Kutta–Joukowski analysis in Sect. 2.2, this is mainly related to differences in the blade axial induction a_B.

For the lower loading conditions listed in Table 3, the corresponding results are not repeated, since detailed straight-blade comparisons were already reported in Li et al. (2025a).

9.2 Swept blades

This section examines the sweep-only blades mB-1 (backward sweep) and mB-5 (forward sweep) to assess the effect of the updated coupling-factor calculation. These two cases were studied in detail in Li et al. (2025a), but are repeated here because the present paper uses an updated coupling-factor calculation, where the area-weighted method (a) is retained but the residual is evaluated for an auxiliary planar reference rotor with straight blades, as described in Sect. 7. Therefore, these cases provide

https://doi.org/10.5194/wes-2026-85
Preprint. Discussion started: 18 June 2026

eawe european academy of wind energy
Open Access WIND ENERGY SCIENCE DISCUSSIONS

a direct test of the updated coupling-factor formulation for backward and forward sweep before it is applied to the prebent and combined curved blade cases. Only the 8 m s^{-1} high-loading condition is repeated here, since the lower-loading cases were already reported in Li et al. (2025a) and the induction effects relevant to the coupling-factor calculation become less significant as the rotor loading decreases.

For the cases considered here, the updated version of method (a), based on a corresponding planar reference rotor with straight blades, is used for all coupled models. With this common coupling-factor procedure, differences between the coupled models mainly reflect the far-wake representation and the modeling of trailed-wake radial induction, rather than the use of different coupling-factor weighting methods. The load offsets relative to the baseline straight blade are shown in Figs. 8 and 9.

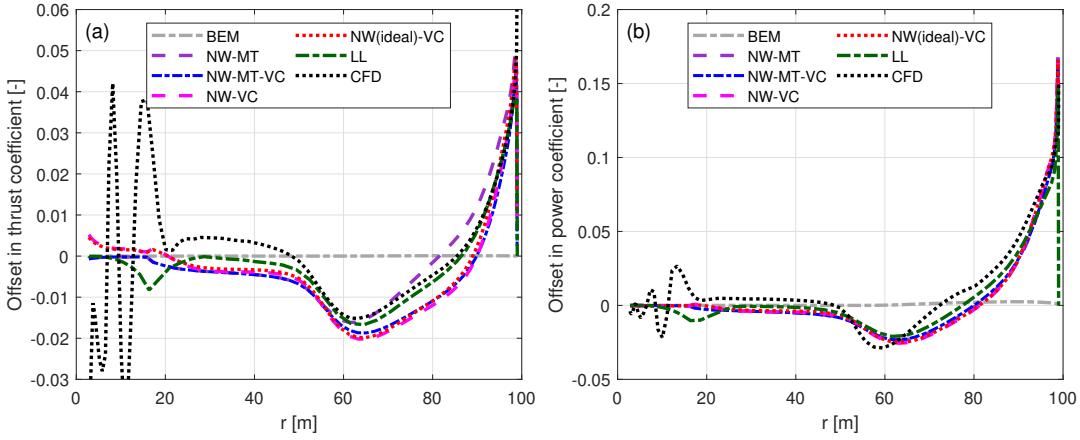

Figure 8. Offset in thrust coefficient (ΔC_t) (a) and simplified power coefficient $(\Delta \tilde{C}_p)$ (b) of the backward swept blade mB-1 compared to the baseline straight blade at a wind speed of 8 m s^{-1}. Results from BEM, NW-MT, NW-MT-VC, NW-VC and NW(ideal)-VC are compared with LL and CFD results.

For both swept blades, LL and CFD show the characteristic sweep-induced load redistribution reported in Li et al. (2025a). For radii below approximately 50 m, the blade main axis remains straight, the load offsets are small and the loads remain close to those of the baseline straight blade. Moving from the blade mid-span toward the blade tip, where the sweep becomes pronounced, a spanwise redistribution of both thrust and power is observed. Specifically, for the backward swept blade mB-1, both thrust and power offsets start to decrease from approximately $r = 50$ m, reaching their largest negative value around $r = 65$ m, and then increase gradually toward the blade tip. Near the tip, the offsets increase sharply and become positive. For the forward swept blade mB-5, a similar spanwise load redistribution pattern is observed, but with the opposite sign. In contrast, the BEM method predicts almost unchanged loads relative to the baseline straight blade. This is expected, since BEM does not model the influence of blade sweep on the wake, and since the chord and twist distributions of the swept blades are modified so that BEM predicts approximately the same baseline loading.

All coupled models reproduce the main sweep-induced load redistribution pattern for both mB-1 and mB-5. The backward swept blade mB-1 represents the case for which the previous coupling-factor calculation was less problematic, for which the coupling factor remains close to that of the corresponding straight blade. Consistently, the coupled models give similar power-

https://doi.org/10.5194/wes-2026-85
Preprint. Discussion started: 18 June 2026

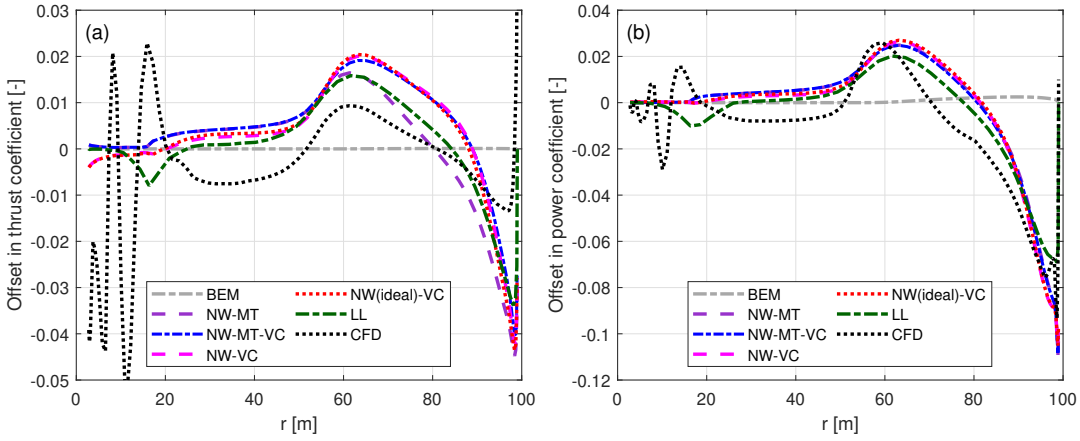

Figure 9. Offset in thrust coefficient (ΔC_t) (a) and simplified power coefficient $(\Delta \tilde{C}_p)$ (b) of the forward swept blade mB-5 compared to the baseline straight blade at a wind speed of 8 m s^{-1}. Results from BEM, NW-MT, NW-MT-VC, NW-VC and NW(ideal)-VC are compared with LL and CFD results.

offset trends and capture the positive power increase toward the blade tip. The main model-to-model difference is observed in the thrust coefficient offset. In particular, NW-MT deviates from NW-MT-VC, NW-VC and NW(ideal)-VC in the outer blade region. In contrast, the simplified power offsets from all coupled models are nearly identical over most of the span. This behavior is consistent with the Kutta–Joukowski analysis in Sect. 2.3: for swept blades, the radial induced velocity contributes directly to the thrust coefficient through the sweep-dependent term, whereas it has no corresponding direct contribution to the simplified power coefficient.

The forward swept blade mB-5 provides a more challenging test of the coupling-factor calculation. In the previous results reported in Li et al. (2025a), this blade showed the strongest sensitivity to the coupling factor. An inaccurate coupling factor is expected to appear mainly as an overall load-level offset, rather than as a fundamentally different redistribution shape, because the rotor-averaged coupling factor affects the far-wake contribution over the blade span. Compared with the previous results reported in Li et al. (2025a), the present results show improved performance for NW-MT and NW-MT-VC even with the simpler area-weighted method (a) applied. With the residual now evaluated for the auxiliary reference rotor, the same area-weighted method (a) can be used consistently for all coupled models considered here. For mB-5, the coupled models therefore recover the load-redistribution trends observed in LL and CFD without the pronounced global offset that was associated with the previous coupling-factor calculation.

Among the coupled models, NW-MT still shows a noticeable difference in the thrust coefficient over the outer blade region, whereas NW-MT-VC, NW-VC and NW(ideal)-VC remain very similar to each other. This is consistent with the fact that NW-MT does not include the trailed-wake contribution to radial induction, which contributes directly to the thrust coefficient for swept blades, as shown by the Kutta–Joukowski analysis in Sect. 2.3. For the simplified power coefficient, all coupled models give very similar predictions over most of the blade span.

https://doi.org/10.5194/wes-2026-85
Preprint. Discussion started: 18 June 2026

eawe european academy of wind energy
Open Access WIND ENERGY SCIENCE DISCUSSIONS

Furthermore, the relative differences in rotor-integrated thrust and power coefficients for the swept blades compared to the baseline straight blade are summarized in Table 4.

Table 4. Relative differences in rotor-integrated thrust and power coefficients of the swept blades mB-1 (backward swept) and mB-5 (forward swept) compared to the baseline straight blade, at a wind speed of 8 m s^{-1}. Relative differences are computed as $\epsilon C_i = (C_i^{\text{swept}} - C_i^{\text{str}})/C_i^{\text{str}}$, where C_i denotes either the thrust coefficient (C_T) or the power coefficient (C_P).

	$\epsilon C_T^{\text{mB-1}}$ [%]	$\epsilon C_T^{\text{mB-5}}$ [%]	$\epsilon C_P^{\text{mB-1}}$ [%]	$\epsilon C_P^{\text{mB-5}}$ [%]
Sweep direction	Backward	Forward	Backward	Forward
BEM	0.01	0.01	0.25	0.25
NW-MT	0.04	-0.10	1.48	-1.06
NW-MT-VC	-0.54	0.51	1.56	-1.15
NW-VC	-0.55	0.44	1.48	-1.34
NW(ideal)-VC	-0.43	0.38	1.61	-1.22
LL	-0.18	0.07	2.20	-1.87
CFD	-0.10	0.12	2.90	-2.68

As shown in Table 4, the rotor-integrated thrust differences caused by sweep are small for all models, with magnitudes below approximately 0.6%. BEM predicts almost no change in rotor-integrated thrust for either swept blade. Since the LL and CFD thrust changes are also small, rotor-integrated thrust alone is not a sensitive measure of the sweep-induced load redistribution. This is consistent with the spanwise results, where positive and negative thrust offsets partly cancel during integration. Nevertheless, NW-MT-VC, NW-VC and NW(ideal)-VC predict the same thrust trends as LL and CFD, namely a small decrease for the backward swept blade mB-1 and a small increase for the forward swept blade mB-5. In contrast, NW-MT predicts the opposite sign for both swept blades, although the magnitude remains small. Therefore, the distributed thrust offsets provide a more meaningful assessment of the swept-blade modeling than the rotor-integrated thrust coefficient alone.

The effect of sweep is more visible in rotor-integrated power. The BEM method predicts a small increase in power for both the backward and forward swept blades. In contrast, the coupled models predict an increase in power for the backward swept blade mB-1 and a decrease in power for the forward swept blade mB-5, consistent with the trends from LL and CFD. Although the coupled models underpredict the magnitude of the power changes compared with LL and CFD, the sign and main trend are recovered.

Together with the local load distributions in Figs. 8 and 9, these results show that the coupled models recover the main sweep-induced load redistribution effects that are missed by BEM. In particular, with the updated method (a), where the coupling-factor residual is evaluated for the auxiliary planar reference rotor with straight blades, the pronounced load-level offset observed in Li et al. (2025a) for NW-MT and NW-MT-VC for the forward swept blade is no longer present. This supports using the same coupling-factor setup for the subsequent prebent and combined-blade cases.

https://doi.org/10.5194/wes-2026-85
Preprint. Discussion started: 18 June 2026

eawe european academy of wind energy
Open Access WIND ENERGY SCIENCE DISCUSSIONS

9.3 Prebent blades

This section examines the prebent blades mW-1 and mW-5 to assess whether the proposed coupled models can reproduce the expected non-planar/prebend behavior. The load offsets relative to the baseline straight blade are shown in Figs. 10 and 11. Results from BEVC and the coupled models NW(ideal)-VC, NW-MT-VC and NW-VC are compared with LL and CFD results, while the BEM method is retained as a baseline reference.

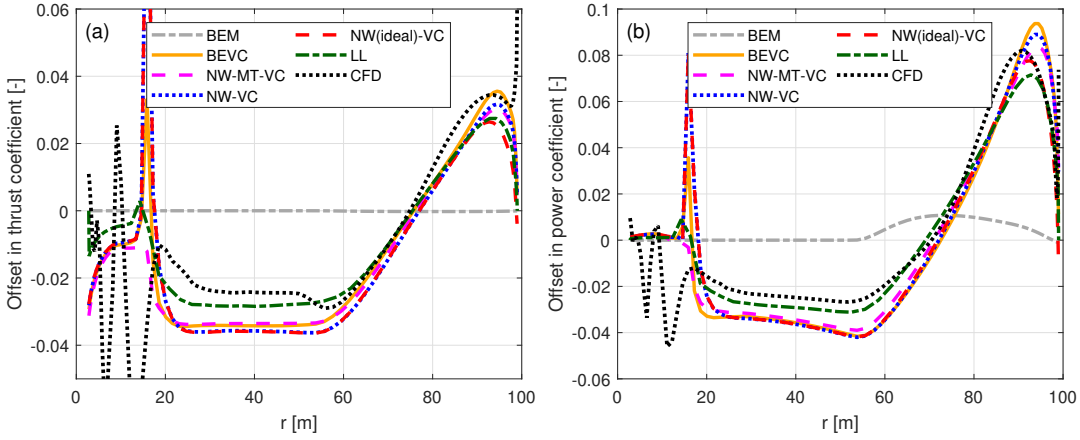

Figure 10. Offset in thrust coefficient (ΔC_t) (a) and simplified power coefficient $(\Delta \tilde{C}_p)$ (b) of the upwind prebent blade mW-1 compared to the baseline straight blade at a wind speed of 8 m s^{-1}. Results from BEM, BEVC, NW-MT-VC, NW-VC and NW(ideal)-VC are compared with LL and CFD results.

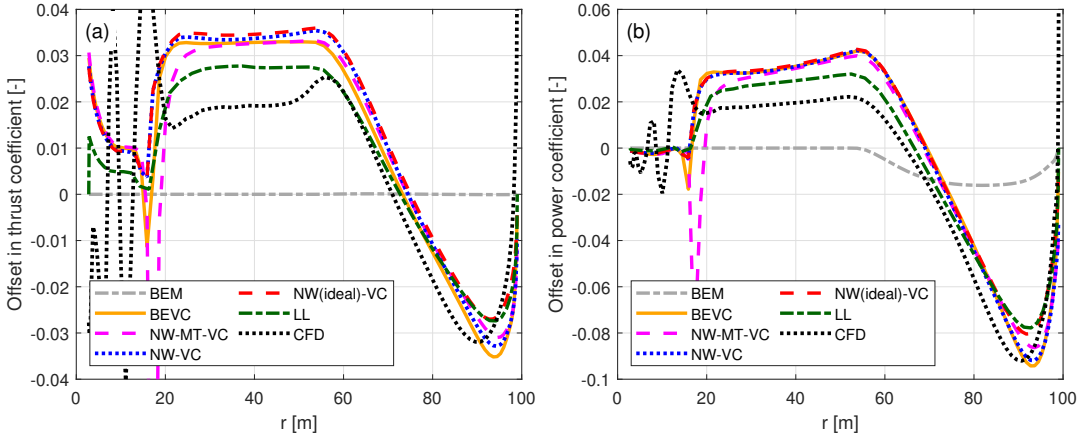

Figure 11. Offset in thrust coefficient (ΔC_t) (a) and simplified power coefficient $(\Delta \tilde{C}_p)$ (b) of the downwind prebent blade mW-5 compared to the baseline straight blade at a wind speed of 8 m s^{-1}. Results from BEM, BEVC, NW-MT-VC, NW-VC and NW(ideal)-VC are compared with LL and CFD results.

https://doi.org/10.5194/wes-2026-85
Preprint. Discussion started: 18 June 2026

eawe european academy of wind energy
Open Access WIND ENERGY SCIENCE DISCUSSIONS

For both prebent blades, the LL and CFD results show a clear load redistribution pattern, consistent with previous findings (Li et al., 2022a, 2025b). For the upwind prebent blade mW-1, the loads are lower than those of the baseline straight blade from $r = 20$ m to $r = 60$ m, with nearly constant offsets over this region. Beyond this region, the offsets increase, cross zero at approximately $r = 75$ m, and become positive toward the blade tip.

For the downwind prebent blade mW-5, a similar load redistribution pattern is observed, but with the opposite sign. In contrast, the BEM method predicts that both prebent blades have approximately the same loads as the baseline straight blade, consistent with the previous study (Li et al., 2025b). Results from BEVC and all coupled models show significant improvement over BEM and capture the load redistribution effect in similarly good agreement with the LL and CFD results. Compared with the coupled models, BEVC tends to overestimate the magnitude of the load offset near the blade tip region around r=90 m. This is likely related to the use of Prandtl's tip-loss correction in the BEVC method, which was developed under planar rotor assumptions (Li et al., 2022a). Results from the simplified coupled models NW-VC and NW-MT-VC are nearly identical, with only small differences for radii larger than 90 m. In the tip region, both simplified models show better agreement with the NW(ideal)-VC model and with the LL results than BEVC. Compared with the simplified coupled models, the NW(ideal)-VC model gives very similar results over most of the blade span, but predicts a smaller magnitude of the load offset in the blade tip region. This difference is likely related to the finite-blade influence on the radial induction. This effect is included in NW(ideal)-VC, whereas the simplified models obtain the radial induction from the vortex cylinder model and therefore do not include this effect. Overall, BEVC, NW-VC and NW-MT-VC all capture the main load redistribution pattern observed in NW(ideal)-VC, LL and CFD.

Furthermore, the relative differences in rotor-integrated thrust and power coefficients for the prebent blades compared to the baseline straight blade are summarized in Table 5.

Table 5. Relative differences in rotor-integrated thrust and power coefficients of the prebent blades mW-1 (upwind prebent) and mW-5 (downwind prebent) compared to the baseline straight blade, at a wind speed of 8 $\mathrm{m\,s^{-1}}$. Relative differences are computed as $\epsilon C_i = (C_i^{\mathrm{prebent}} - C_i^{\mathrm{str}})/C_i^{\mathrm{str}}$, where C_i denotes either the thrust coefficient (C_T) or the power coefficient (C_P).

	$\epsilon C_T^{\mathrm{mW\text{-}1}}$ [%]	$\epsilon C_T^{\mathrm{mW\text{-}5}}$ [%]	$\epsilon C_P^{\mathrm{mW\text{-}1}}$ [%]	$\epsilon C_P^{\mathrm{mW\text{-}5}}$ [%]
Prebend direction	Upwind	Downwind	Upwind	Downwind
BEM	-0.01	0.01	0.15	-0.91
BEVC	-0.62	0.39	1.14	-2.26
NW-MT-VC	-0.78	0.47	1.28	-2.46
NW-VC	-0.82	0.66	1.22	-2.26
NW(ideal)-VC	-0.96	0.84	0.67	-1.57
LL	-0.51	0.31	1.65	-2.93
CFD	-0.13	-0.09	2.47	-4.62

As shown in Table 5, the BEM method predicts only small rotor-integrated differences for both prebent blades and substantially underestimates the power changes predicted by LL and CFD. This is expected, since the BEM method does not model the

https://doi.org/10.5194/wes-2026-85
Preprint. Discussion started: 18 June 2026

wake-induced effects of blade prebend (Li et al., 2025b)[5]. For the rotor-integrated power coefficient, BEVC, NW-MT-VC and NW-VC all improve substantially over BEM. The average absolute error relative to LL is reduced from approximately 1.8% for BEM to about 0.6% for BEVC, 0.4% for NW-MT-VC, and 0.6% for NW-VC. For the rotor-integrated thrust coefficient, the improvement is less uniform. BEVC and NW-MT-VC are closer to LL than BEM, whereas NW-VC predicts somewhat larger prebend-induced thrust changes, especially for the downwind prebent blade mW-5. The differences between NW-VC and NW-MT-VC are mainly related to their different far-wake representations.

In comparison, the CFD results show larger quantitative differences from LL and from all engineering aerodynamic models. This is likely related to the use of 2-D airfoil data in all models except CFD, whereas the CFD solver resolves the full 3-D flow field.

It is important to note that the improvement of BEVC and the coupled models over BEM is more pronounced for the distributed loads than for the rotor-integrated quantities. This is because the load redistribution effect due to prebend is partially canceled out when the loads are integrated along the blade span.

9.3.1 Lower loading conditions

For the lower loading conditions, the results are shown in Figs. B1 and B2 in Appendix B, while the main conclusions are summarized here.

For all lower loading conditions, the BEM method predicts that the prebent blades have approximately the same loads as the baseline straight blade, again confirming that the BEM method is not able to model the influence of blade prebend.

In contrast, BEVC and the two simplified coupled models NW-VC and NW-MT-VC remain close over most of the span, although local differences become more visible at the lowest loading condition. In comparison, NW(ideal)-VC shows larger differences from these models for radii larger than about 60 m. This is likely related to the finite blade influence on the radial induction, which is included in NW(ideal)-VC but not in the the simplified coupled models. As a result, NW(ideal)-VC generally remains closer to the LL results in the outer blade region, highlighting the importance of accurate modeling of radial induction.

In the tip region, the apparent differences between the models become visually more pronounced as the rotor loading decreases. This should be interpreted with care, because the absolute prebend-induced load offsets also become smaller at lower loading. The maximum absolute error in the local thrust coefficient remains small, being approximately 4×10^{-3} at 12 m s^{-1}, decreasing to 2×10^{-3} at 15 m s^{-1} and 1×10^{-3} at 20 m s^{-1}. At 20 m s^{-1}, the prebend-induced offsets are therefore very small. Since each offset is obtained by subtracting the corresponding straight blade result from the prebent blade result within the same method, small numerical or post-processing differences in either calculation can have a relatively large influence on the plotted offset. These small absolute errors indicate that the simplified models remain suitable for efficient engineering predictions of spanwise aerodynamic load redistribution over the range of rotor-loading conditions considered here.

[5] As described in Sect. 8.4, the chord and twist distributions of the curved blades are modified so that the BEM method predicts the same bound circulation distribution as for the baseline straight blade, which in turn results in approximately the same thrust and only small changes in power.

https://doi.org/10.5194/wes-2026-85
Preprint. Discussion started: 18 June 2026

eawe european academy of wind energy
Open Access WIND ENERGY SCIENCE DISCUSSIONS

9.4 Blades with combined sweep and prebend

This section examines blades with combined sweep and prebend, which provide a demanding test of the unified framework developed here, since neither the sweep-only nor the prebend-only model branch can capture the full aerodynamic behavior. The four blades considered here fall into two groups. For mC-11 (backward sweep, upwind prebend) and mC-55 (forward sweep, downwind prebend), the load redistribution effects induced by sweep and prebend act in the same direction and therefore reinforce each other, leading to a larger redistribution magnitude. For mC-15 (backward sweep, downwind prebend) and mC-51 (forward sweep, upwind prebend), the load redistribution effects induced by sweep and prebend act in opposite directions and therefore partially cancel.

The BEM method serves as the baseline reference, since it does not model either sweep or prebend effects. In addition, BEVC and NW-MT are included as single-effect reference models for the prebend/non-planar branch and the sweep branch, respectively. The proposed coupled models NW(ideal)-VC, NW-VC and NW-MT-VC, which include both sweep and prebend effects, are compared against higher-fidelity LL and CFD results.

For blades mC-11 and mC-55, results at the optimal operating condition of 8 m s^{-1} are shown in Figs. 12 and 13.

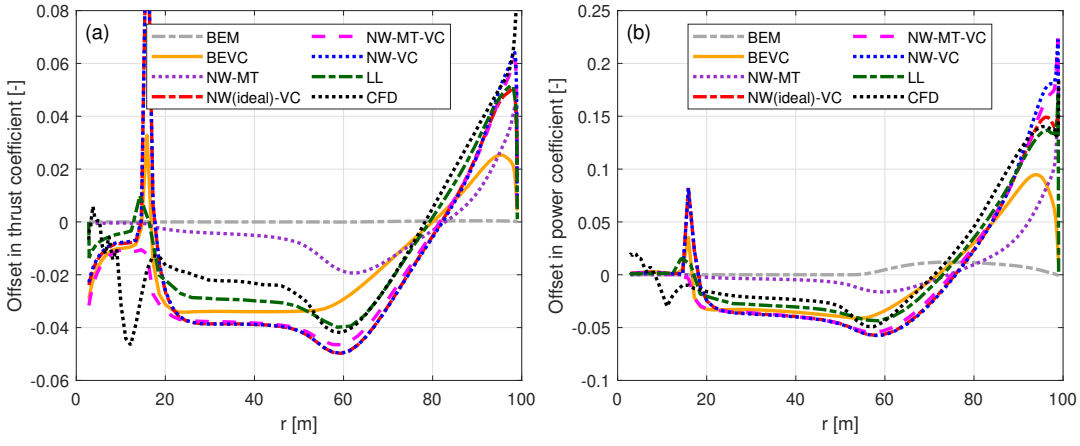

Figure 12. Offset in thrust coefficient (ΔC_t) (a) and simplified power coefficient ($\Delta \tilde{C}_p$) (b) of blade mC-11 with backward sweep and upwind prebend compared to the baseline straight blade at a wind speed of 8 m s^{-1}. Results from BEM, BEVC, NW-MT, NW-MT-VC, NW-VC and NW(ideal)-VC are compared with LL and CFD results.

For blades mC-11 and mC-55, LL and CFD results show a pronounced load redistribution pattern, consistent with previous findings (Li et al., 2022a, 2025b). For blade mC-11, with backward sweep and upwind prebend, the loads are lower than those of the baseline straight blade from the blade root to a radius of approximately 80 m and higher from there to the blade tip. For blade mC-55, with forward sweep and downwind prebend, a similar load redistribution pattern is observed, but with opposite signs.

As expected, the BEM method predicts nearly the same loads for mC-11 and mC-55 as for the baseline straight blade, since it does not account for either sweep or prebend effects. The single-effect models BEVC and NW-MT reproduce the correct load

https://doi.org/10.5194/wes-2026-85
Preprint. Discussion started: 18 June 2026

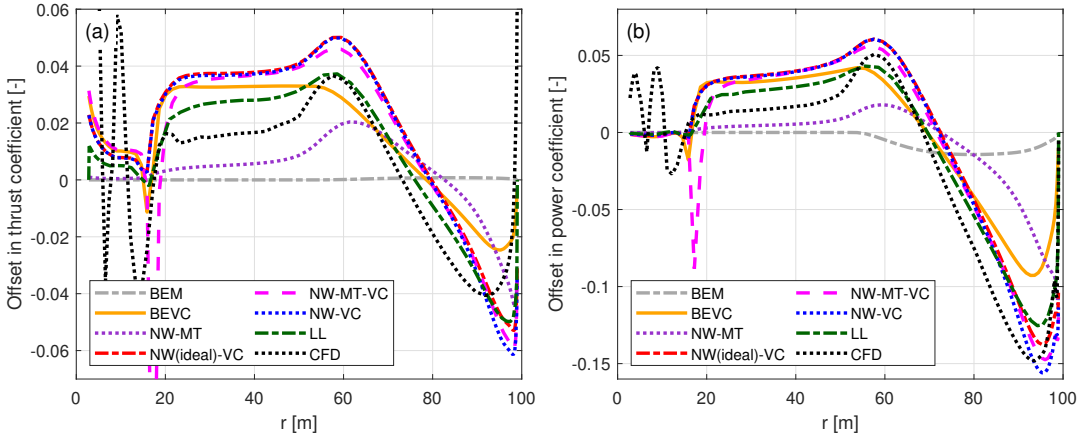

Figure 13. Offset in thrust coefficient (ΔC_t) (a) and simplified power coefficient $(\Delta \tilde{C}_p)$ (b) of blade mC-55 with forward sweep and downwind prebend compared to the baseline straight blade at a wind speed of 8 m s^{-1}. Results from BEM, BEVC, NW-MT, NW-MT-VC, NW-VC and NW(ideal)-VC are compared with LL and CFD results.

redistribution trends, but underestimate their magnitudes because they account for only prebend or only sweep, respectively. The idealized coupled model NW(ideal)-VC shows good agreement with the LL results and matches the main trends observed in CFD. The simplified coupled models NW-VC and NW-MT-VC also agree well with NW(ideal)-VC and LL. As for the prebent blades, these remaining tip region discrepancies are mainly related to neglecting the influence of the finite number of blades on the radial induction.

For blades mC-15 and mC-51, results at the optimal operating condition of 8 m s^{-1} are shown in Figs. 14 and 15.

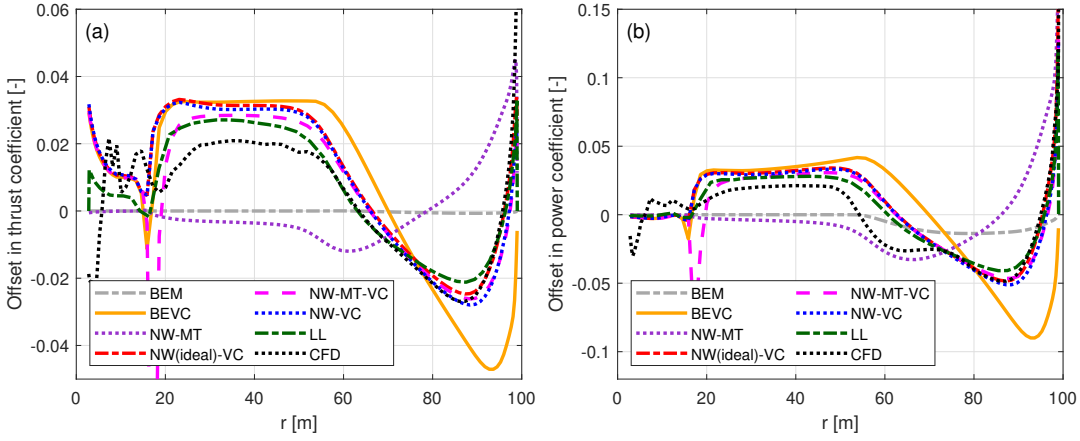

Figure 14. Offset in thrust coefficient (ΔC_t) (a) and simplified power coefficient $(\Delta \tilde{C}_p)$ (b) of the blade mC-15 with backward sweep and downwind prebend compared to the baseline straight blade at a wind speed of 8 m s^{-1}. Results from BEM, BEVC, NW-MT, NW-MT-VC, NW-VC and NW(ideal)-VC are compared with LL and CFD results.

https://doi.org/10.5194/wes-2026-85
Preprint. Discussion started: 18 June 2026

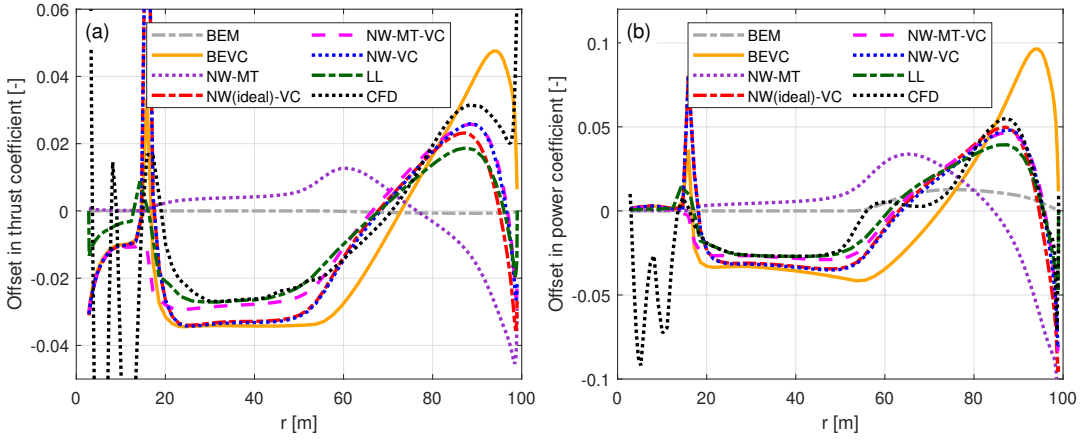

Figure 15. Offset in thrust coefficient (ΔC_t) (a) and simplified power coefficient $(\Delta \tilde{C}_p)$ (b) of the blade mC-51 with forward sweep and upwind prebend compared to the baseline straight blade at a wind speed of 8 $\mathrm{m\,s^{-1}}$. Results from BEM, BEVC, NW-MT, NW-MT-VC, NW-VC and NW(ideal)-VC are compared with LL and CFD results.

For blades mC-15 and mC-51, where sweep and prebend act in opposite directions, LL and CFD results show a more complex redistribution pattern because the two effects partially cancel. For blade mC-15, with backward sweep and downwind prebend, the load offsets are positive from approximately $r = 20$ m to $r = 70$ m and negative from about $r = 70$ m to $r = 95$ m. In the blade tip region, for $r > 95$ m, the offsets increase sharply and become positive again. For blade mC-51, with forward sweep and upwind prebend, a similar redistribution pattern is observed, but with opposite signs.

Again, the BEM method predicts almost the same loads as for the baseline straight blade. For these two blades, BEVC and NW-MT clearly illustrate the limitation of single-effect engineering models: sweep and prebend effects must be modeled together. The BEVC method, which neglects sweep effects, captures the correct load redistribution pattern over much of the span because prebend dominates there. However, it overestimates the magnitude of the load offsets for radii beyond 80 m, where sweep effects become dominant. In contrast, the NW-MT method, which models only sweep effects, predicts load offsets in the opposite direction compared to LL and CFD results over most of the span. Only in the outermost tip region, with $r > 95$ m, do sweep effects dominate and reverse the sign of the load offset. For both mC-15 and mC-51, the idealized coupled model NW(ideal)-VC shows very good agreement with LL and CFD, as it models both sweep and prebend effects. The simplified coupled models NW-VC and NW-MT-VC also agree well with NW(ideal)-VC, LL and CFD. They remain close to each other over most of the blade span, indicating that the difference between the far-wake modeling is small for these combined cases. The remaining discrepancies are mainly located near the blade tip and are due to the simplified treatment of radial induction and the separate modeling of sweep and prebend effects.

In summary, the simplified coupled models are based on two approximations: sweep and prebend effects are modeled separately and then superimposed, and the radial induction model does not include finite-blade effects. The good agreement

https://doi.org/10.5194/wes-2026-85
Preprint. Discussion started: 18 June 2026

eawe european academy of wind energy
Open Access WIND ENERGY SCIENCE DISCUSSIONS

between the idealized and simplified coupled models at the optimal condition indicates that these approximations work well for the cases considered here.

Furthermore, the relative differences in rotor-integrated thrust and power coefficients for the curved blades compared to the baseline straight blade are summarized in Tables 6 and 7.

Table 6. Relative differences in rotor-integrated thrust coefficient of the curved blades compared to the baseline straight blade, at a wind speed of 8 m s^{-1}. Relative differences are computed as $\epsilon C_T = (C_T^{\text{curved}} - C_T^{\text{str}})/C_T^{\text{str}}$.

	$\epsilon C_T^{\text{mC-11}}$ [%]	$\epsilon C_T^{\text{mC-55}}$ [%]	$\epsilon C_T^{\text{mC-15}}$ [%]	$\epsilon C_T^{\text{mC-51}}$ [%]
Sweep	Backward	Forward	Backward	Forward
Prebend	Upwind	Downwind	Downwind	Upwind
BEM	0.03	0.05	-0.02	-0.03
BEVC	-1.11	1.02	-0.26	-0.06
NW-MT	-0.14	0.16	0.24	-0.34
NW-MT-VC	-1.35	0.87	-0.04	-0.14
NW-VC	-1.33	1.04	0.09	-0.35
NW(ideal)-VC	-1.42	1.24	0.40	-0.53
LL	-0.71	0.34	0.10	-0.32
CFD	-0.36	-0.10	-0.12	0.19

Table 7. Relative differences in rotor-integrated power coefficients of the curved blades compared to the baseline straight blade, at a wind speed of 8 m s^{-1}. Relative differences are computed as $\epsilon C_P = (C_P^{\text{curved}} - C_P^{\text{str}})/C_P^{\text{str}}$.

	$\epsilon C_P^{\text{mC-11}}$ [%]	$\epsilon C_P^{\text{mC-55}}$ [%]	$\epsilon C_P^{\text{mC-15}}$ [%]	$\epsilon C_P^{\text{mC-51}}$ [%]
Sweep	Backward	Forward	Backward	Forward
Prebend	Upwind	Downwind	Downwind	Upwind
BEM	0.34	-0.71	-0.63	0.44
BEVC	1.42	-2.14	-1.90	1.33
NW-MT	1.76	-2.10	0.71	-0.90
NW-MT-VC	2.66	-3.92	-0.60	0.35
NW-VC	2.73	-3.74	-0.59	-0.18
NW(ideal)-VC	1.99	-2.86	0.20	-0.33
LL	3.70	-4.84	-0.33	0.27
CFD	5.69	-6.78	-2.27	-0.38

As shown in Table 6, the rotor-integrated thrust differences are generally smaller than the corresponding power differences in Table 7, but they are not negligible. For blades mC-11 and mC-55, where sweep and prebend act in the same direction, NW-MT-VC and NW-VC predict the correct trends in both rotor-integrated thrust and power. For the power coefficient, they also provide

https://doi.org/10.5194/wes-2026-85
Preprint. Discussion started: 18 June 2026

clear improvements over BEM, BEVC and NW-MT, although noticeable differences relative to the LL results remain. For the thrust coefficient, the coupled models predict the same sign as LL, but they do not show a systematic improvement compared with the existing engineering models. For blades mC-15 and mC-51, the rotor-integrated quantities are more difficult to assess. In these two cases, the load redistributions due to sweep and prebend act in opposite directions and are partially canceled out when integrated over the span. This is also evident from the LL results, for which both the rotor-integrated thrust and power changes are close to zero. As a result, even a model that does not correctly represent the local wake-induced effects associated with sweep and prebend may appear to perform well in terms of integrated quantities alone. This explains why BEM predicts the rotor-integrated loads surprisingly well for mC-15 and mC-51, despite failing to predict the local load distributions.

The proposed coupled models NW-MT-VC and NW-VC therefore do not show the same clear advantage over BEM in rotor-integrated quantities for mC-15 and mC-51 as they do for mC-11 and mC-55. However, they still capture the local load redistribution much more accurately, which is a more relevant measure of model performance.

As already noted in the interpretation of the model comparisons, LL and CFD are used as complementary references with different roles. The coupled engineering models are therefore assessed mainly by whether they recover the dominant spanwise load-redistribution trends, rather than by exact agreement with CFD.

9.4.1 Lower loading conditions

For the lower loading conditions, the results are shown in Figs. B3 to B6 in Appendix B, while the main conclusions are summarized below.

For all lower loading conditions, the BEM method again predicts approximately the same loads for the curved blades as for the baseline straight blade. For the blades mC-11 and mC-55, LL and CFD show load redistribution patterns similar to those at the optimal operating condition. For the blades mC-15 and mC-51, the load redistribution patterns observed in LL and CFD results are more complicated compared to mC-11 and mC-55. The single-effect models BEVC and NW-MT remain insufficient for the combined curved blades. For mC-11 and mC-55 they underestimate the load redistribution magnitude, while for mC-15 and mC-51 they are not able to predict the correct load redistribution pattern. Compared with the optimal operating condition, the relative importance of the sweep effect increases as rotor loading decreases. The idealized coupled model NW(ideal)-VC continues to show good agreement with LL and CFD. The simplified coupled models NW-MT-VC and NW-VC remain almost identical, with small offsets relative to NW(ideal)-VC. As shown in Li et al. (2025b), the error introduced due to modeling sweep and prebend effects separately and then superimposing them is rather small. Therefore, the remaining difference between the idealized and simplified coupled models is mainly associated with the effect of the finite number of blades on the radial induction near the blade tip. These errors are small in absolute terms. The absolute error in thrust coefficient is less than 5×10^{-3} at 12 m s^{-1}, 2×10^{-3} at 15 m s^{-1} and 1×10^{-3} at 20 m s^{-1}. This indicates that the simplified models remain sufficiently accurate for efficient engineering predictions of spanwise aerodynamic load redistribution over the range of rotor-loading conditions considered here.

https://doi.org/10.5194/wes-2026-85
Preprint. Discussion started: 18 June 2026

eawe european academy of wind energy
Open Access WIND ENERGY SCIENCE DISCUSSIONS

10 Conclusions and future work

The present study closes a capability gap in engineering aerodynamic modeling by establishing a unified framework for general curved wind turbine blades and coned rotors that combine sweep and prebend. To this end, an idealized model, NW(ideal)-VC, was introduced as the highest-fidelity realization of the proposed framework before practical simplifications are introduced. Motivated by prior computational fluid dynamics (CFD) results showing that blade sweep and prebend effects can be modeled separately and then superimposed with good accuracy, two simplified engineering models, NW-VC and NW-MT-VC, were developed for practical applications. In both simplified models, sweep effects are represented through the bound vortex and the near wake helical trailed vortex, whereas prebend, coning, and other non-planar effects are represented by the vortex cylinder model.

Comparisons with higher-fidelity free-wake lifting line (LL) and Reynolds-averaged Navier–Stokes (RANS) simulations show that the proposed coupled models capture the load redistribution caused by blade curvature with good accuracy over a range of operating conditions. For swept blades, the results confirm that the updated coupling factor calculation preserves the previously observed sweep-induced load redistribution while reducing the pronounced load-level offset found for the forward swept case. For prebent blades, the proposed coupled models show similarly good agreement as BEVC with the higher-fidelity results. For blades that combine sweep and prebend, the advantages of the unified framework become much more evident: the conventional BEM method does not capture the induced load redistribution, whereas BEVC and NW-MT capture only part of the effect and may even predict the wrong spanwise redistribution pattern. The results also show that accurate rotor-integrated loads can hide large errors in the local spanwise load distribution, highlighting the importance of distributed load comparisons. The remaining differences are mainly related to the modeling of radial induction near the blade tip, particularly the influence of the finite number of blades. In the simplified models, these tip-region differences are small in absolute terms for the operating conditions considered, which supports their use in engineering applications. At the same time, the remaining differences between LL and CFD results highlight the inherent limitations of engineering models based on 2-D airfoil data when compared with fully resolved 3-D flow simulations. Although the computational cost of the simplified models is higher than that of the blade element momentum (BEM) method, it remains orders of magnitude lower than that of LL and CFD, making the models attractive for iterative design optimization and well suited for time-domain aero-servo-elastic simulations. The formulation can be seamlessly extended to account for blade deflections during aeroelastic simulations.

Future work should focus on improving the radial induction model. In the simplified formulations, the main prebend effects are included, whereas the influence of the finite number of blades and of blade sweep on the radial induction is not yet represented. Since the present study is limited to steady-state cases, future work should also investigate unsteady effects within the proposed framework. Integrating the NW-MT-VC model into aero-servo-elastic simulation tools and further refining its dynamic response would expand its practical applicability.

https://doi.org/10.5194/wes-2026-85
Preprint. Discussion started: 18 June 2026

eawe european academy of wind energy
Open Access WIND ENERGY SCIENCE DISCUSSIONS

Data availability. The 2-D airfoil data used in this article are generated with 2-D fully turbulent RANS computations (Bortolotti et al., 2019).

Appendix A: Nomenclature

A1 Roman-letter variables used in the present work

Symbol	Description
a, a_{B}, a_∞	axial induction factor; axial induction factor at the blade section; annulus-averaged axial induction factor
a'	tangential induction factor
$A_{a,i}$	annulus area of section i
c	chord length
C_L	lift coefficient
C_t	local thrust coefficient
$\tilde{C}_p$	simplified local power coefficient from the tangential force
C_T, C_P	rotor-integrated thrust and power coefficients
f	local aerodynamic force per unit span
F	Prandtl's tip-loss factor
F_a	area-weighted residual function used in the coupling-factor calculation
h	radial distance between trailing point and calculation point
k_{FW}	rotor-averaged coupling factor
k_s	normalized sectional circulation of the vortex cylinder
N_{B}	number of blades
N_{cp}	number of calculation points
N_{tp}	number of trailing points
r, R	radius of the calculation point; radius of the trailing point
s, $\mathrm{d}s$	curved blade length, differential curved blade length
$\boldsymbol{t}$, $\boldsymbol{t}^*$	tangent vector, modified tangent vector
$\mathbf{T}$	transformation matrix
u_a, u_t, u_r	axial, tangential, and radial induced velocities
$\tilde{u}_a$, $\tilde{u}_r$, $\tilde{u}_{t,l}$	vortex cylinder influence functions
U_0	free-stream wind speed
V_{rel}	2-D relative velocity magnitude
$\boldsymbol{W}$	steady-state near-wake induced velocity
y, y_{FW}	axial position; axial position of the far-wake vortex cylinder

https://doi.org/10.5194/wes-2026-85
Preprint. Discussion started: 18 June 2026

eawe european academy of wind energy
Open Access WIND ENERGY SCIENCE DISCUSSIONS

A2 Greek-letter variables used in the present work

Symbol	Description
β	trailed-vortex azimuthal angle
Γ_{B}, Γ	bound circulation strength of one blade; total bound circulation strength of all blades
γ_t, γ_l	tangential and longitudinal vorticity strengths of the vortex cylinder
δ	position angle
δa	axial induction residual used in the coupling-factor calculation
Δa_{VC}, $\Delta a'_{\mathrm{VC}}$	non-planar axial and tangential induction corrections from the vortex cylinder model
ΔC_t, $\Delta \tilde{C}_p$	offsets in local thrust and simplified local power coefficients relative to the straight blade
Δy_{FW}	downstream shift distance of the far-wake vortex cylinders
η, $\tilde{\eta}$	axial offset between trailing and calculation points and its normalized form
$\hbar_{\mathrm{NW}}$	rotor-averaged near-wake helical pitch
κ, κ^*	dihedral angle and effective dihedral angle
λ, λ_r	rotor tip-speed ratio and local speed ratio
ρ	air density
θ_p	pitch angle
φ	inflow angle
ψ, ψ^*	sweep angle and effective sweep angle
Ω	rotor rotational speed

https://doi.org/10.5194/wes-2026-85
Preprint. Discussion started: 18 June 2026

eawe european academy of wind energy
Open Access WIND ENERGY SCIENCE DISCUSSIONS

A3 Subscripts used in the present work

Symbol	Description
a, t, r	axial, tangential, radial direction
l	longitudinal vortex contribution
B	blade or value at the blade
BEM	value from the BEM method
CFD	value from the CFD solver
KJ	value from the Kutta–Joukowski analysis
NW	near-wake contribution
FW	far-wake contribution
MT	momentum theory
VC	vortex cylinder model
bound	bound-vortex contribution
trail	trailed-vortex contribution
tot	total value
i	blade section or calculation point index
j	trailing point index

A4 Superscripts used in the present work

Symbol	Description
pl	planar rotor
np	non-planar rotor
pl,str	planar reference rotor with straight blades
str	straight blade
t	Newton iteration step

https://doi.org/10.5194/wes-2026-85
Preprint. Discussion started: 18 June 2026

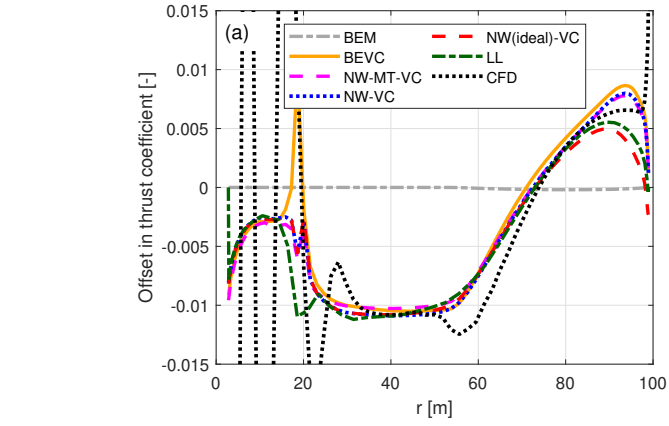

eawe european academy of wind energy
Open Access WIND ENERGY SCIENCE DISCUSSIONS

Appendix B: Comparison of the results for low loadings

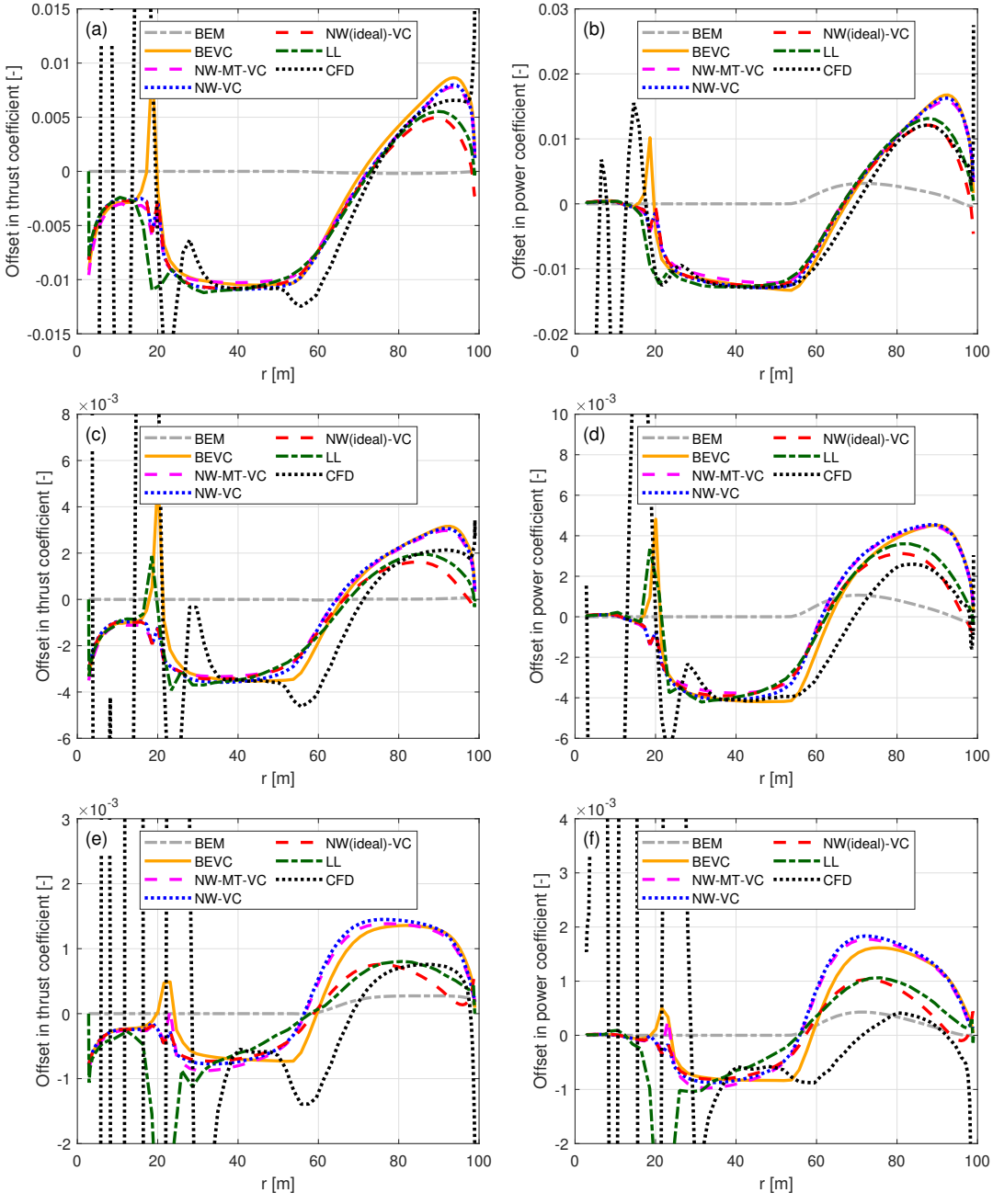

Figure B1. Offset in thrust coefficient (ΔC_t) and simplified power coefficient ($\Delta \tilde{C}_p$) of the upwind prebent blade mW-1 compared to the baseline straight blade. Results from BEM, BEVC, NW-MT-VC, NW-VC and NW(ideal)-VC are compared with LL and CFD results. Results are shown for three operational conditions: (a, b) at 12 m s^{-1}; (c, d) at 15 m s^{-1}; and (e, f) at 20 m s^{-1}.

https://doi.org/10.5194/wes-2026-85
Preprint. Discussion started: 18 June 2026

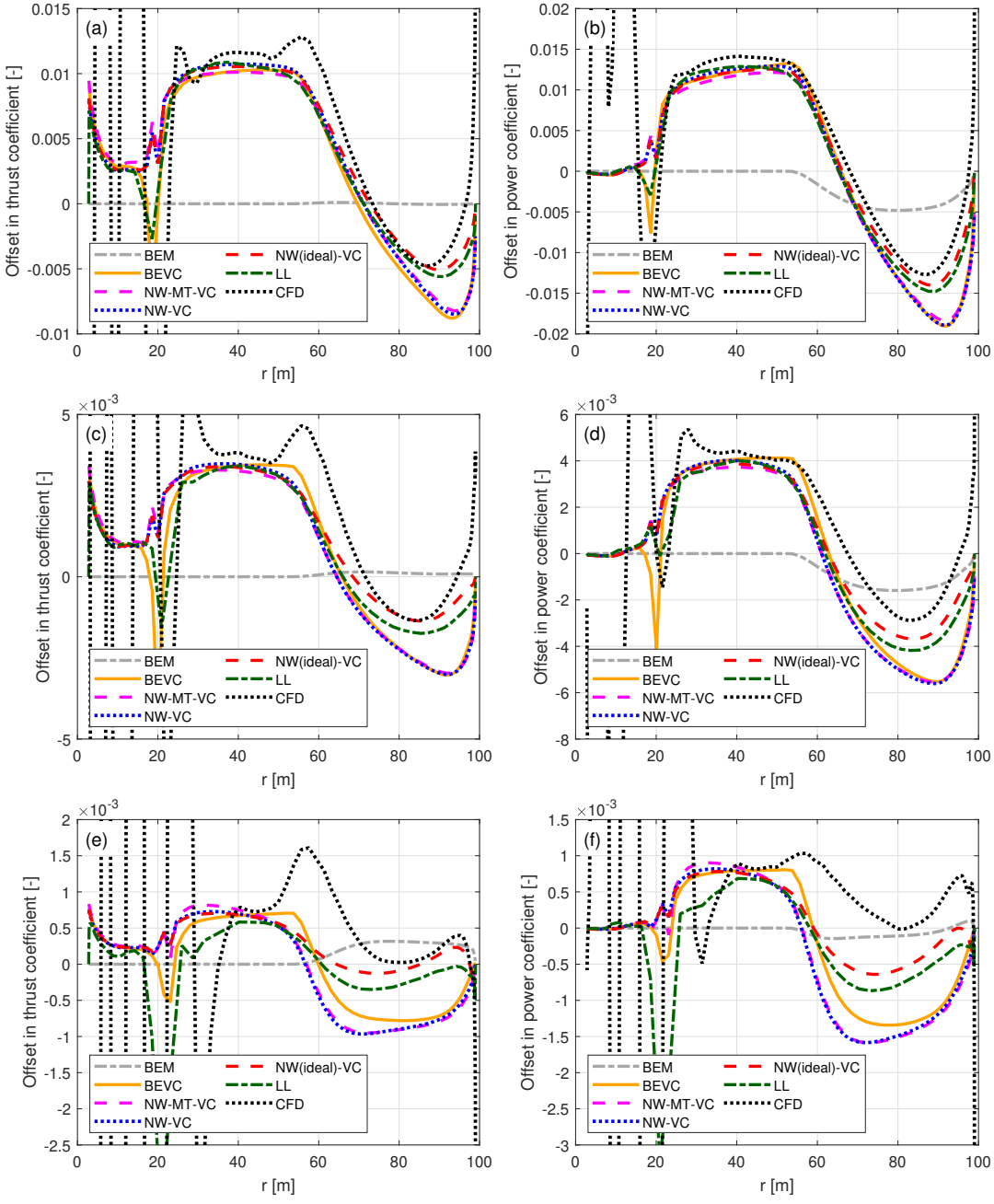

Figure B2. Offset in thrust coefficient (ΔC_t) and simplified power coefficient ($\Delta \tilde{C}_p$) of the downwind prebent blade mW-5 compared to the baseline straight blade. Results from BEM, BEVC, NW-MT-VC, NW-VC and NW(ideal)-VC are compared with LL and CFD results. Results are shown for three operational conditions: (a, b) at 12 m s^{-1}; (c, d) at 15 m s^{-1}; and (e, f) at 20 m s^{-1}.

https://doi.org/10.5194/wes-2026-85
Preprint. Discussion started: 18 June 2026

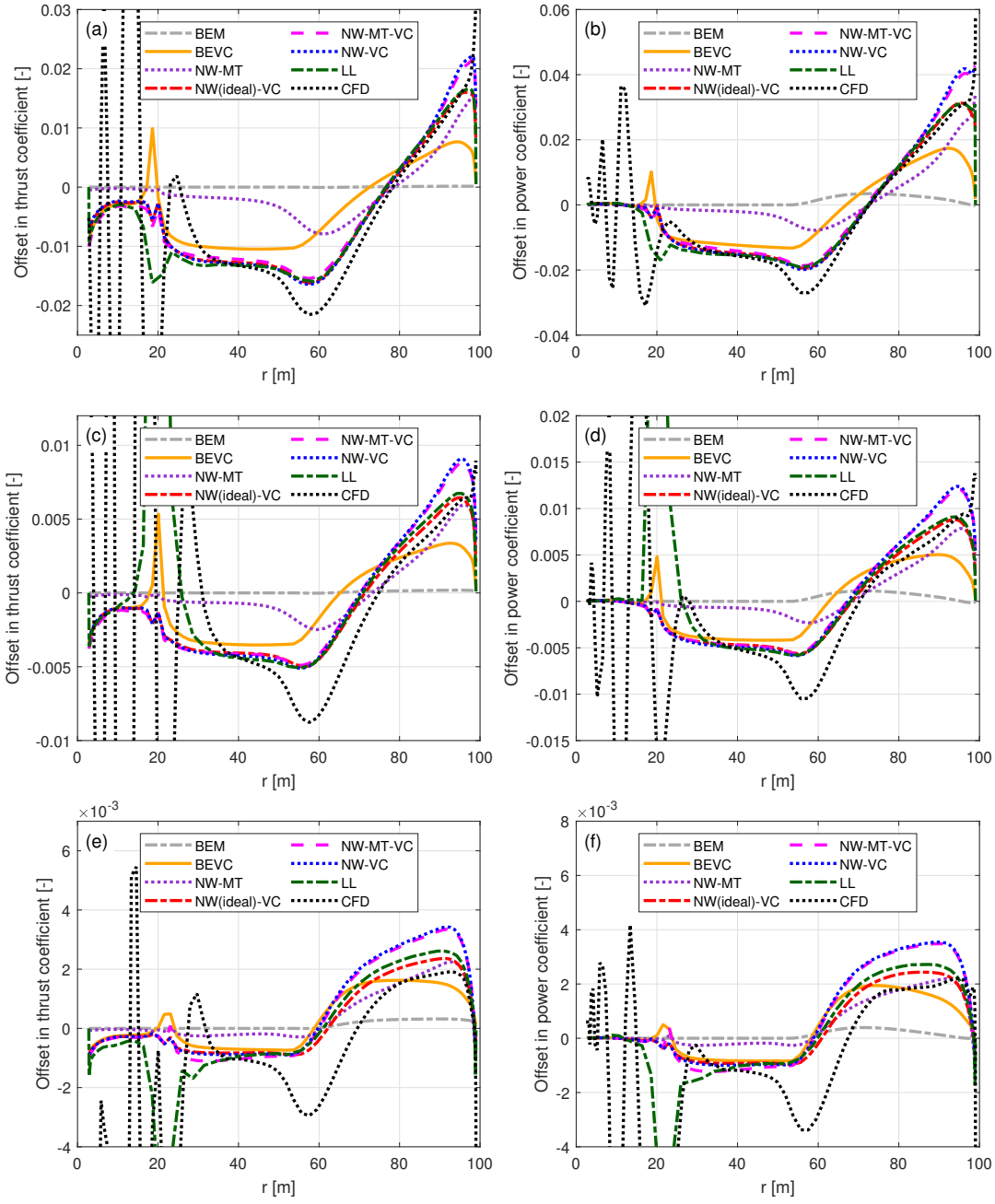

Figure B3. Offset in thrust coefficient (ΔC_t) and simplified power coefficient ($\Delta \tilde{C}_p$) of blade mC-11 with backward sweep and upwind prebend compared to the baseline straight blade. Results from BEM, BEVC, NW-MT, NW-MT-VC, NW-VC and NW(ideal)-VC are compared with LL and CFD results. Results are shown for two operational conditions: (a, b) at 12 m s^{-1} and (c, d) at 15 m s^{-1}.

https://doi.org/10.5194/wes-2026-85
Preprint. Discussion started: 18 June 2026

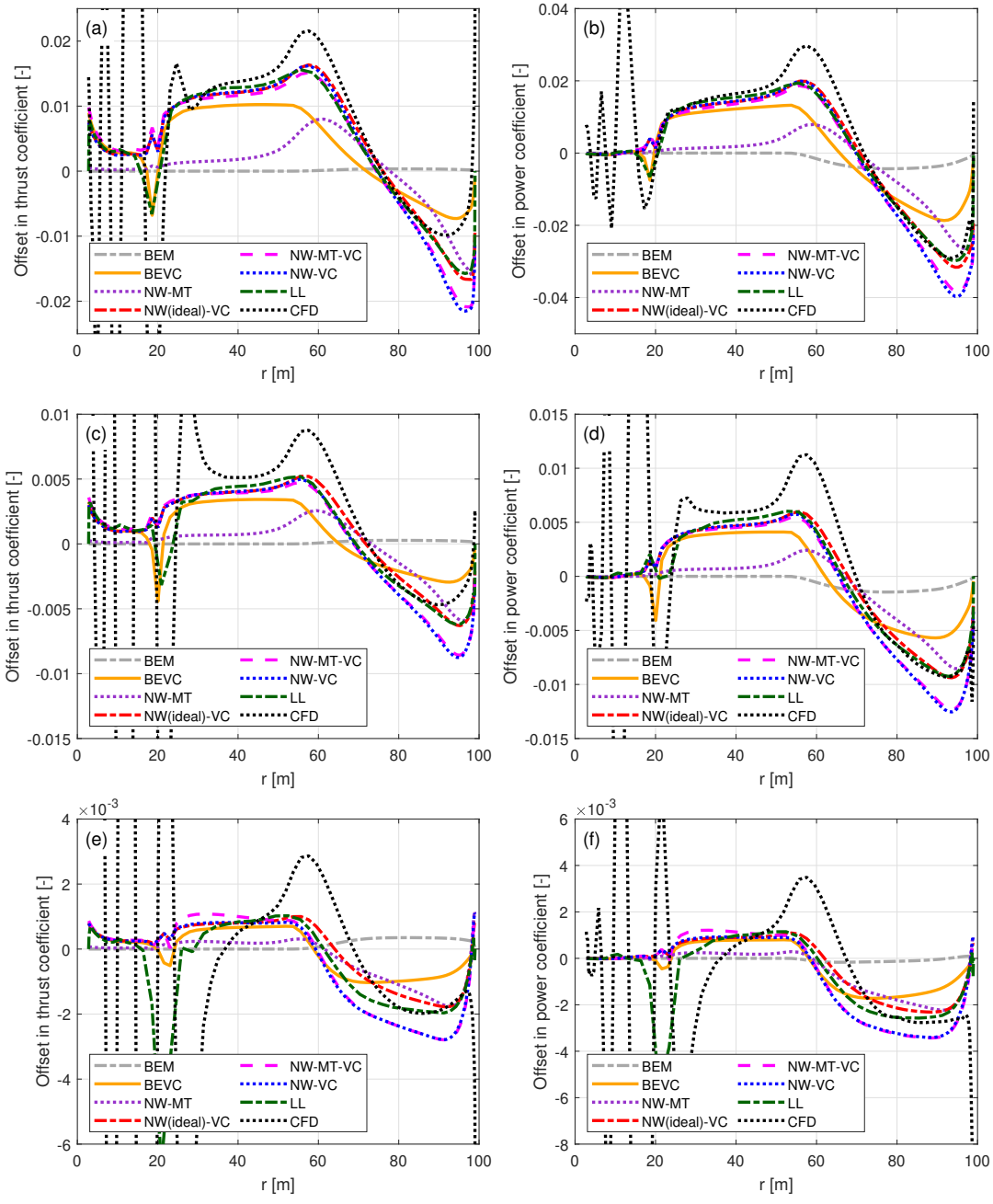

Figure B4. Offset in thrust coefficient (ΔC_t) and simplified power coefficient ($\Delta \tilde{C}_p$) of blade mC-55 with forward sweep and downwind prebend compared to the baseline straight blade. Results from BEM, BEVC, NW-MT, NW-MT-VC, NW-VC and NW(ideal)-VC are compared with LL and CFD results. Results are shown for two operational conditions: (a, b) at 12 m s^{-1} and (c, d) at 15 m s^{-1}.

https://doi.org/10.5194/wes-2026-85
Preprint. Discussion started: 18 June 2026

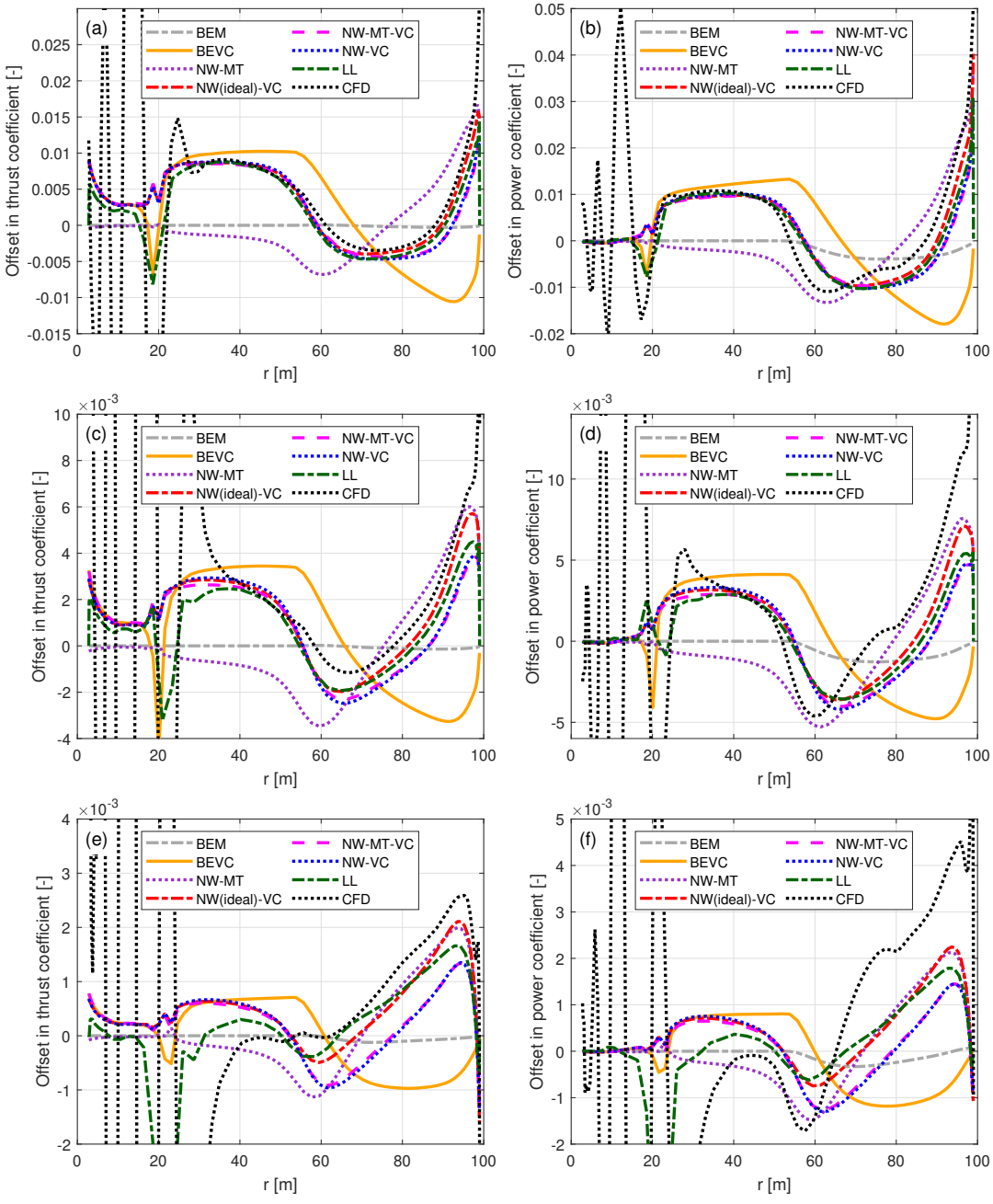

Figure B5. Offset in thrust coefficient (ΔC_t) and simplified power coefficient ($\Delta \tilde{C}_p$) of blade mC-15 with backward sweep and downwind prebend compared to the baseline straight blade. Results from BEM, BEVC, NW-MT, NW-MT-VC, NW-VC and NW(ideal)-VC are compared with LL and CFD results. Results are shown for two operational conditions: (a, b) at 12 m s^{-1} and (c, d) at 15 m s^{-1}.

https://doi.org/10.5194/wes-2026-85
Preprint. Discussion started: 18 June 2026

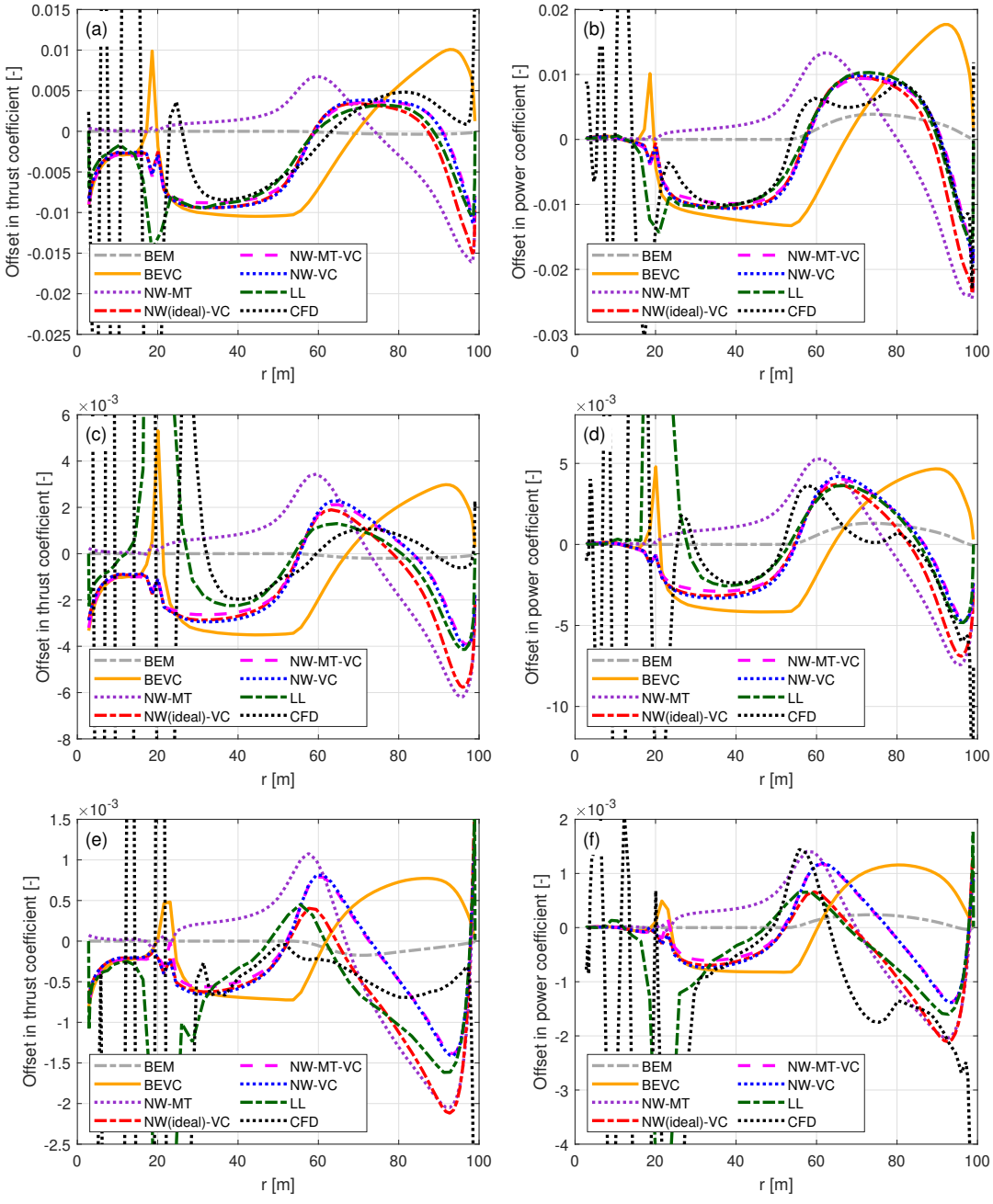

Figure B6. Offset in thrust coefficient (ΔC_t) and simplified power coefficient $(\Delta \tilde{C}_p)$ of blade mC-51 with forward sweep and upwind prebend compared to the baseline straight blade. Results from BEM, BEVC, NW-MT, NW-MT-VC, NW-VC and NW(ideal)-VC are compared with LL and CFD results. Results are shown for two operational conditions: (a, b) at 12 m s^{-1} and (c, d) at 15 m s^{-1}.

https://doi.org/10.5194/wes-2026-85
Preprint. Discussion started: 18 June 2026

eawe european academy of wind energy
Open Access WIND ENERGY SCIENCE DISCUSSIONS

Author contributions. This work builds on previous research by AL, GRP and MG. The concept of coupling the near wake and far wake vortex cylinder model originated from AL, MG and GRP. The idealized and simplified coupled near and far wake models were proposed and described by AL, with contributions from MG and GRP. The close similarity between the NW-MT-VC and NW-VC models in modeling non-planar/prebend effects was identified and described by AL, with contributions from MG and GRP. The concept of using a planar reference rotor with straight blades for the coupling factor was suggested by GRP during discussions with AL and MG, and was further developed by AL. AL performed numerical simulations using the RANS CFD solver, the free-wake lifting line solver and engineering aerodynamic models. AL also post-processed the results and prepared the figures. All authors discussed the results and jointly contributed to the conclusions and to the writing of this manuscript.

Competing interests. DTU Wind and Energy Systems develops and distributes the Navier–Stokes solver EllipSys3D on commercial and academic terms. DTU Wind and Energy Systems also develops, supports and distributes HAWC2 on commercial terms, and HAWC2 is available free of charge for educational and academic research purposes.

Acknowledgements. The authors would like to thank Frederik Zahle of DTU Wind and Energy Systems for his valuable contributions to establishing the fully-scripted mesh generation and post-processing workflows for the Navier–Stokes simulations in EllipSys3D. Computational and data resources were provided by the Sophia HPC Cluster at DTU (https://doi.org/10.57940/fafc-6m81, DTU, 2019). This research has been supported by the AMTip project, funded by the Energy Technology Development and Demonstration Programme (EUDP) (Case no. 64021-2062). Additionally, this research was supported by the Floatfarm project, a Horizon Europe R&I Action (HORIZON-CL5-2023-D3-01-05), supported by the European Climate, Infrastructure and Environment Executive Agency (CINEA). Earlier versions of this paper were revised iteratively with the assistance of AI tools, including OpenAI's ChatGPT (GPT-4, GPT-4o, o1, GPT-4.1, GPT-4.5, o3, GPT-5, GPT-5.4, and GPT-5.5). These tools were used by the authors to generate suggestions for improving language and wording based on author-prepared drafts that were developed and updated throughout the preparation of the paper. The paper underwent multiple rounds of revision by the authors, with AI-generated suggestions being selectively incorporated and extensively modified.

https://doi.org/10.5194/wes-2026-85
Preprint. Discussion started: 18 June 2026

eawe european academy of wind energy
Open Access WIND ENERGY SCIENCE DISCUSSIONS

References

Andersen, P. B., Gaunaa, M., Zahle, F., and Madsen, H. A.: A near wake model with far wake effects implemented in a multi body aero-servo-elastic code, in: Proceedings of the European Wind Energy Conference and Exhibition 2010 (EWEC 2010), pp. 387–431, Warsaw, Poland, ISBN 9781617823107, 2010.

Barlas, T., Ramos-García, N., Pirrung, G. R., and González Horcas, S.: Surrogate-based aeroelastic design optimization of tip extensions on a modern 10 MW wind turbine, Wind Energy Science, 6, 491–504, https://doi.org/10.5194/wes-6-491-2021, 2021.

Barlas, T., Pirrung, G. R., Ramos-García, N., González Horcas, S., Li, A., and Madsen, H. A.: Atmospheric rotating rig testing of a swept blade tip and comparison with multi-fidelity aeroelastic simulations, Wind Energy Science, 7, 1957–1973, https://doi.org/10.5194/wes-7-1957-2022, 2022.

Bortolotti, P., Tarrés, H. C., Dykes, K., Merz, K., Sethuraman, L., Verelst, D., and Zahle, F.: IEA Wind TCP Task 37: Systems Engineering in Wind Energy – WP2.1 Reference Wind Turbines, Tech. Rep. NREL/TP-5000-73492, National Renewable Energy Laboratory (NREL), Golden, CO, USA, https://www.nrel.gov/docs/fy19osti/73492.pdf, 2019.

Branlard, E. and Gaunaa, M.: Superposition of vortex cylinders for steady and unsteady simulation of rotors of finite tip-speed ratio, Wind Energy, 19, 1307–1323, https://doi.org/10.1002/we.1899, 2015a.

Branlard, E. and Gaunaa, M.: Cylindrical vortex wake model: right cylinder, Wind Energy, 18, 1973–1987, https://doi.org/10.1002/we.1800, 2015b.

Crawford, C.: Re-examining the precepts of the blade element momentum theory for coning rotors, Wind Energy, 9, 457–478, https://doi.org/10.1002/we.197, 2006.

Dicholkar, A., Zahle, F., and Sørensen, N. N.: Convergence enhancement of SIMPLE-like steady-state RANS solvers applied to airfoil and cylinder flows, Journal of Wind Engineering and Industrial Aerodynamics, 220, 104 863, https://doi.org/10.1016/j.jweia.2021.104863, 2022.

Dicholkar, A., Lønbæk, K., Madsen, M. H. A., Zahle, F., and Sørensen, N. N.: From bluff bodies to optimal airfoils: Numerically stabilized RANS solvers for reliable shape optimization, Aerospace Science and Technology, 161, 110 153, https://doi.org/10.1016/j.ast.2025.110153, 2025.

Fritz, E. K., Ferreira, C., and Boorsma, K.: An efficient blade sweep correction model for blade element momentum theory, Wind Energy, 25, 1977–1994, https://doi.org/10.1002/we.2778, 2022.

Glauert, H.: Airplane Propellers, in: Aerodynamic Theory: A General Review of Progress, Vol. IV, Division L, edited by Durand, W. F., pp. 169–360, Springer, Berlin / New York, 1935.

Hoerner, S. F. and Borst, H. V.: Fluid-dynamic lift: practical information on aerodynamic and hydrodynamic lift, LA Hoerner, ISBN 978-9998831636, 1985.

Horcas, S. G., Ramos-García, N., Li, A., Pirrung, G., and Barlas, T.: Comparison of aerodynamic models for horizontal axis wind turbine blades accounting for curved tip shapes, Wind Energy, 26, 5–22, https://doi.org/10.1002/we.2780, 2023.

Jonkman, J. and Sprague, M.: OpenFAST Documentation Release v3.0.0, Golden, CO, USA, 2021.

Larsen, T. and Hansen, A.: How 2 HAWC2, the user's manual, no. 1597(ver. 3-1)(EN) in Denmark. Forskningscenter Risø. Risø-R, Risø National Laboratory, ISBN 978-87-550-3583-6, 2007.

https://doi.org/10.5194/wes-2026-85
Preprint. Discussion started: 18 June 2026

Larwood, S. M. and Zutek, M.: Swept wind turbine blade aeroelastic modeling for loads and dynamic behavior, in: WINDPOWER 2006 Conference in Pittsburgh, USA, 4–7 June 2006. https://scholarlycommons.pacific.edu/soecs-facpres/4/ (last access: 15 October 2025), 2006.

Li, A., Pirrung, G., Madsen, H. A., Gaunaa, M., and Zahle, F.: Fast trailed and bound vorticity modeling of swept wind turbine blades, Journal of Physics: Conference Series, 1037, 062 012, https://doi.org/10.1088/1742-6596/1037/6/062012, 2018.

Li, A., Gaunaa, M., Pirrung, G. R., Ramos-García, N., and Horcas, S. G.: The influence of the bound vortex on the aerodynamics of curved wind turbine blades, Journal of Physics: Conference Series, 1618, 052 038, https://doi.org/10.1088/1742-6596/1618/5/052038, 2020.

Li, A., Gaunaa, M., Pirrung, G. R., and Horcas, S. G.: A computationally efficient engineering aerodynamic model for non-planar wind turbine rotors, Wind Energy Science, 7, 75–104, https://doi.org/10.5194/wes-7-75-2022, 2022a.

Li, A., Gaunaa, M., Pirrung, G. R., Meyer Forsting, A., and Horcas, S. G.: How should the lift and drag forces be calculated from 2-D airfoil data for dihedral or coned wind turbine blades?, Wind Energy Science, 7, 1341–1365, https://doi.org/10.5194/wes-7-1341-2022, 2022b.

Li, A., Pirrung, G. R., Gaunaa, M., Madsen, H. A., and Horcas, S. G.: A computationally efficient engineering aerodynamic model for swept wind turbine blades, Wind Energy Science, 7, 129–160, https://doi.org/10.5194/wes-7-129-2022, 2022c.

Li, A., Gaunaa, M., Pirrung, G. R., and Lønbæk, K.: How does the blade element momentum method see swept or prebent blades?, Journal of Physics: Conference Series, 2767, 022 033, https://doi.org/10.1088/1742-6596/2767/2/022033, 2024.

Li, A., Gaunaa, M., and Pirrung, G. R.: Computationally efficient aerodynamic modelling of swept wind turbine blades using coupled near-wake and vortex cylinder models, Wind Energy Science, 10, 2515–2550, https://doi.org/10.5194/wes-10-2515-2025, 2025a.

Li, A., Gaunaa, M., Pirrung, G. R., and Lønbæk, K.: Disentangling wake and projection effects in the aerodynamics of wind turbines with curved blades, Wind Energy Science, 10, 2299–2349, https://doi.org/10.5194/wes-10-2299-2025, 2025b.

Li, A., Gaunaa, M., and Pirrung, G. R.: Internet Appendix for: "Computationally efficient aerodynamic modeling of curved wind turbine blades and non-planar rotors using coupled near wake and vortex cylinder models", https://doi.org/10.5281/zenodo.20067772, Internet Appendix, 2026.

Liebst, B. S.: Wind turbine gust load alleviation utilizing curved blades, Journal of Propulsion and Power, 2, 371–377, https://doi.org/10.2514/3.22897, 1986.

Madsen, H. A. and Rasmussen, F.: A near wake model for trailing vorticity compared with the blade element momentum theory, Wind Energy, 7, 325–341, https://doi.org/10.1002/we.131, 2004.

Madsen, H. A., Larsen, T. J., Pirrung, G. R., Li, A., and Zahle, F.: Implementation of the blade element momentum model on a polar grid and its aeroelastic load impact, Wind Energy Science, 5, 1–27, https://doi.org/10.5194/wes-5-1-2020, 2020a.

Madsen, H. A., Zahle, F., Meng, F., Barlas, T., Rasmussen, F., and Rudolf, R. T.: Initial performance and load analysis of the LowWind turbine in comparison with a conventional turbine, Journal of Physics: Conference Series, 1618, 032 011, https://doi.org/10.1088/1742-6596/1618/3/032011, 2020b.

Manolas, D. I., Serafeim, G. P., Chaviaropoulos, P. K., Riziotis, V. A., and Voutsinas, S. G.: Assessment of load reduction capabilities using passive and active control methods on a 10 MW-scale wind turbine, Journal of Physics: Conference Series, 1037, 032 042, https://doi.org/10.1088/1742-6596/1037/3/032042, 2018.

Menter, F. R.: Two-equation eddy-viscosity turbulence models for engineering applications, AIAA Journal, 32, 1598–1605, https://doi.org/10.2514/3.12149, 1994.

Okulov, V. L., Sørensen, J. N., and Wood, D. H.: The rotor theories by Professor Joukowsky: Vortex theories, Progress in Aerospace Sciences, 73, 19–46, https://doi.org/10.1016/j.paerosci.2014.10.002, 2015.

https://doi.org/10.5194/wes-2026-85
Preprint. Discussion started: 18 June 2026

Pirrung, G., Madsen, H. A., Kim, T., and Heinz, J.: A coupled near and far wake model for wind turbine aerodynamics, Wind Energy, 19, 2053–2069, https://doi.org/10.1002/we.1969, 2016.

Ramos-García, N., Sørensen, J. N., and Shen, W. Z.: Three-dimensional viscous-inviscid coupling method for wind turbine computations, Wind Energy, 19, 67–93, https://doi.org/10.1002/we.1821, 2016.

Ramos-García, N., Hejlesen, M. M., Sørensen, J. C., and Walther, J. H.: Hybrid vortex simulations of wind turbines using a three-dimensional viscous–inviscid panel method, Wind Energy, 20, 1871–1889, https://doi.org/10.1002/we.2126, 2017.

Sørensen, J. N.: General Momentum Theory for Horizontal Axis Wind Turbines, vol. 4 of *Research Topics in Wind Energy*, Springer International Publishing, ISBN 978-3-319-22114-4, https://doi.org/10.1007/978-3-319-22114-4, 2016.

Zuteck, M.: Adaptive blade concept assessment: curved platform induced twist investigation, Tech. rep., Sandia National Laboratories, Albuquerque, NM, USA, https://doi.org/10.2172/803289, 2002.